


Monazite behaviour during isothermal decompression in pelitic granulites: a case study from Dinggye, Tibetan Himalaya

Jia-Min Wang^{1,2}  · Fu-Yuan Wu^{1,3} · Daniela Rubatto⁴ · Shi-Ran Liu⁵ · Jin-Jiang Zhang⁵ · Xiao-Chi Liu¹ · Lei Yang¹

Received: 5 February 2017 / Accepted: 16 August 2017
© Springer-Verlag GmbH Germany 2017

Abstract Monazite is a key accessory mineral for metamorphic geochronology, but interpretation of its complex chemical and age zoning acquired during high-temperature metamorphism and anatexis remains a challenge. We investigate the petrology, pressure–temperature and timing of metamorphism in pelitic and psammitic granulites that contain monazite from the Greater Himalayan Crystalline Complex (GHC) in Dinggye, southern Tibet. These rocks underwent isothermal decompression from pressure of >10 kbar to ~5 kbar at temperatures of 750–830 °C, and recorded three metamorphic stages at kyanite (M_1), sillimanite (M_2) and cordierite-spinel grade (M_3). Monazite and zircon crystals were dated by microbeam techniques either as grain separates or in thin sections. U–Th–Pb ages are linked to specific conditions of mineral growth on the basis

of zoning patterns, trace element signatures, index mineral inclusions (melt inclusions, sillimanite and K-feldspar) in dated domains and textural relationships with co-existing minerals. The results show that inherited domains (500–400 Ma) are preserved in monazite even at granulite-facies conditions. Few monazites or zircon yield ages related to the M_1 -stage (~30–29 Ma), possibly corresponding to prograde melting by muscovite dehydration. During the early stage of isothermal decompression, inherited or prograde monazites in most samples were dissolved in the melt produced by biotite dehydration-melting. Most monazite grains crystallized from melt toward the end of decompression (M_3 -stage, 21–19 Ma) and are chemically related to garnet breakdown reactions. Another peak of monazite growth occurred at final melt crystallization (~15 Ma), and these monazite grains are unzoned and are homogeneous in composition. In a regional context, our pressure–temperature–time data constrains peak high-pressure metamorphism within the GHC to ~30–29 Ma in Dinggye Himalaya. Our results are in line with a melt-assisted exhumation of the GHC rocks.

Communicated by Timothy L. Grove.

Electronic supplementary material The online version of this article (doi:10.1007/s00410-017-1400-y) contains supplementary material, which is available to authorized users.

✉ Jia-Min Wang
wangjiamin@mail.iggcas.ac.cn

¹ State Key Laboratory of Lithospheric Evolution, Institute of Geology and Geophysics, Chinese Academy of Sciences, 100029 Beijing, China

² Institut für Geologie Mineralogie und Geophysik, Ruhr-Universität Bochum, 44780 Bochum, Germany

³ Center for Excellence in Tibetan Plateau Earth Sciences, Chinese Academy of Sciences, 100101 Beijing, China

⁴ Institute of Geological Sciences, University of Bern, 3012 Bern, Switzerland

⁵ School of Earth and Space Sciences, Peking University, 100871 Beijing, China

Keywords U–Th–Pb geochronology · Monazite · Isothermal decompression · Granulite-facies · Himalaya

Introduction

Monazite ($\text{Ce, La, Th}\text{PO}_4$) is a common accessory mineral in metapelitic or metapsammitic rocks, and is frequently used for geochronology of metamorphic terranes. It has several strengths in dating amphibolite- and granulite-facies metamorphism. (a) Monazite generally has high concentrations of U (0.1–0.4 wt%) and Th (2–12 wt%), and low initial Pb contents (e.g. Parrish 1990), making it suitable for U–Th–Pb determinations with high spatial resolution via various

techniques such as ion microprobe (e.g. Harrison et al. 1995), electron microprobe (EPMA, e.g. Williams et al. 2007) and laser ablation–(multi-collector) inductively coupled plasma–mass spectrometry (LA-(MC)ICP-MS, Cottle et al. 2009a). (b) Pb diffusion in monazite at dry conditions is very slow (Cherniak et al. 2004) and monazite has high retentivity for radiogenic Pb even at >1000 °C (Seydoux-Guillaume et al. 2002). (c) During a metamorphic cycle, monazite may grow at various stages such as sub-solidus prograde conditions (e.g., Wing et al. 2003; Kohn et al. 2005), anatexis (e.g., Rubatto et al. 2001, 2013; Bhowmik et al. 2014; Harley and Nandakumar 2014; Dumond et al. 2015; Wang et al. 2015a), and during retrograde fluid alteration (e.g. Williams et al. 2011; Kelly et al. 2012; Taylor et al. 2014; Grand'Homme et al. 2016) or, to a less extent, during high-temperature deformation (Erickson et al. 2015). This variability in monazite growth conditions enables the extraction of time information at various points along a pressure–temperature (P–T) trajectory but also constitutes a challenge for age interpretation.

In high-temperature migmatites, monazite ages can be very complex and multiple ages can be preserved in samples collected from one tectonic unit (e.g., Simpson et al. 2000; Kohn et al. 2005; Rubatto et al. 2013; Harley and Nandakumar 2014; Wang et al. 2015a). Interpretation of monazite ages relies on a thorough understanding of monazite behaviour during metamorphism, which is still limited. Most studies agree that monazite solubility in melt is sufficiently high that during high-temperature partial melting, pre-existing monazite grains are dissolved and new monazite crystallizes when light rare earth element (LREE) saturation is reached. Through this process, monazite could record ages of prograde melting, peak metamorphism or melt crystallization upon cooling depending on local saturation reached in melt pockets (e.g., Seydoux-Guillaume et al. 2002; Rubatto et al. 2013; Bhowmik et al. 2014; Harley and Nandakumar 2014; Taylor et al. 2016). However, studies by phase equilibria modelling propose that solubility of monazite in melt is sufficiently high that monazite will be continuously dissolved in granitic melt along the up-temperature prograde path; therefore, monazite is more likely to grow during melt crystallization upon cooling (Kelsey et al. 2008; Yakymchuk and Brown 2014).

These studies give rise to the following questions: (a) can monazite form during prograde melting or peak metamorphism; (b) what processes/reactions trigger monazite growth during partial melting; (c) how can monazite survive subsequent partial melting if it grows over prograde or peak conditions? For cases that underwent prolonged partial melting or sustained high-temperatures metamorphism, preservation of these peak-stage monazites will even be more difficult.

An important aspect in investigating monazite behaviour during high-temperature metamorphism is to

establish the link between metamorphic reactions and monazite growth/crystallization. Many reactions have been proposed for sub-solidus monazite growth (e.g., Smith and Barreiro 1990; Akers et al. 1993; Kingsbury et al. 1993; Pyle et al. 2001; Catlos et al. 2002; Wing et al. 2003; Kohn et al. 2005; Janots et al. 2007), but only selected cases have linked monazite growth to reactions during partial melting (Rubatto et al. 2013; Dumond et al. 2015). Therefore, more studies are required to understand the link between melting reactions (e.g., muscovite and biotite dehydration-melting reactions) and monazite growth or trace elements signatures during anatexis of crustal rocks.

The Greater Himalayan Crystalline Complex (GHC) provides an excellent natural laboratory for studying monazite behaviour during high-temperature anatexis. The Himalayan orogenic process—on-going collision of India with Asia—has not been overprinted by later orogenic events. Himalayan metamorphic ages (<50 – 55 Ma, Leech et al. 2005; Rowley 1996) are relatively young so that in situ geochronology (0.5–2% precision) can accurately distinguish different metamorphic stages within a P–T cycle, which may not be resolvable for older orogenic belts. The GHC exposes similar sequences of amphibolite- to granulite-facies metapelitic or metapsammitic rocks along the ~ 2400 km Himalayan strike (e.g., Warren et al. 2011; Zhang et al. 2013; Kohn 2014; Mottram et al. 2014), and P–T–time determination results can be compared spatially.

The Dinggye region of Tibetan Himalaya exposes a spectacular variety of pelitic and psammitic granulites of the GHC that underwent isothermal decompression at peak temperatures (e.g., Borghi et al. 2003). In the Dinggye region, some of the deepest buried GHC rocks along the strike of the Himalayas are exposed and this is thus an ideal site for studying the monazite behaviour during high-temperature metamorphism. In this study, P–T paths were calculated for the investigated samples to provide more precise constraints on the conditions of monazite growth. Monazite U–Th–Pb ages of nine samples were determined using LA–ICP–MS and linked to specific metamorphic stages. The P–T–time link was achieved by comprehensive constraints of monazite zoning patterns, index mineral inclusions in dated monazite, textural correlations with surrounding minerals, and chemical compositions of monazite. Zircon U–Pb ages were also determined by ion microprobe to better interpret monazite ages. The obtained information allows summarizing monazite behaviour within a granulite-facies P–T cycle and potential melting reactions that account for monazite dissolution-growth processes. In a regional context, the P–T–time information of the investigated granulites is compared to the high-pressure mafic granulite exposed in the Dinggye Himalaya and considered with respect to the possible mechanism that triggered the exhumation of the GHC.

Geological setting

General geology of the central Himalaya

The Himalayan orogen is commonly divided from north to south into the Tethyan Himalayan Sequence (THS), GHC, Lesser Himalayan Sequence (LHS) and Siwalik Group (SG, Fig. 1). These units are separated by the South Tibetan Detachment (STD), Main Central Thrust (MCT), Main Boundary Thrust and Main Frontier Thrust. Within the Himalayan sequences, the GHC represents the metamorphic core, which is mainly composed of amphibolite- to granulite-facies metasedimentary rocks (e.g., Searle et al. 2003; Goscombe et al. 2006; Kohn 2008; Groppo et al. 2009; Imayama et al. 2010; Wang et al. 2013, 2015a), Early Paleozoic orthogneiss (e.g., Cawood et al. 2007; Wang et al. 2012) and Oligocene–Miocene leucogranite (e.g., Harrison et al. 1995; Searle et al. 1997, 2003; Visonà and Lombardo 2002; Carosi et al. 2013; Leloup et al. 2015; Wu et al. 2015). The STD is a low-angle normal-sense shear zone that generally dips to the north and extends over 2400 km along the

Himalayan strike (e.g., Burchfiel et al. 1992; Searle et al. 2003; Cottle et al. 2007; Leloup et al. 2010). The MCT is a top-to-the-south thrust-sense ductile shear zone and separates the hanging-wall GHC rocks from the footwall greenschist-facies to lower-amphibolite-facies LHS rocks (e.g., Arita 1983; Schelling 1992; Harrison et al. 1998; Kohn 2008; Searle et al. 2008; Wang et al. 2015b). It has been suggested that exhumation of the GHC was assisted by coeval movement along the STD and MCT during early to mid Miocene (e.g., Burchfiel and Royden 1985; Burchfiel et al. 1992; Searle et al. 2003, 2005). However, recent studies highlight the contribution of several new tectono-metamorphic discontinuities within the core of the GHC—the High Himalayan discontinuities (Fig. 1)—that were active coevally with the STD, but predated the MCT (Carosi et al. 2010; Larson et al. 2013, 2015; Montomoli et al. 2013, 2015; Wang et al. 2016) and the diachronous exhumation of different GHC blocks (Kohn et al. 2004; Corrie and Kohn 2011; Imayama et al. 2012; Rubatto et al. 2013; Cottle et al. 2015; Wang et al. 2015a; Chakraborty et al. 2016), which have forced alternative burial-exhumation models.

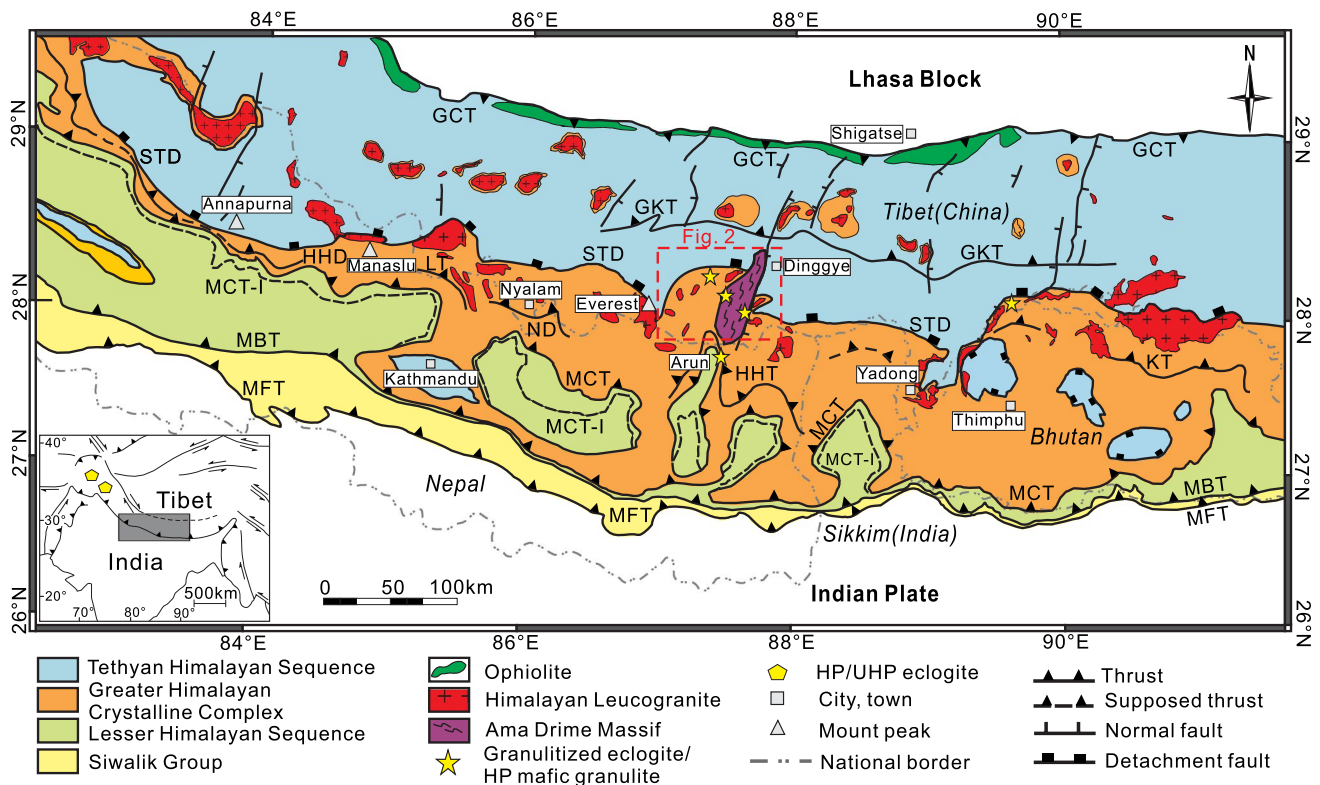


Fig. 1 Simplified geological map of the central and eastern Himalayas (modified after Wang et al. 2016; Yin 2006). GCT Greater Central Thrust, STD South Tibetan detachment, MCT Main Central Thrust, MBT Main Boundary Thrust, MFT Main Frontier Thrust, HHD High Himalayan Discontinuity, LT Langtang Thrust,

ND Nyalam Discontinuity, HHT High Himal Thrust, KT Kakhtang Thrust, GKT Gyirong-Kangmar Thrust. Granulitized eclogites or high-pressure mafic granulites are from: Bhutan, Grujic et al. (2011), Warren et al. (2011); Arun river valley, Corrie et al. (2010); see Fig. 2 for those from the Dinggye region

Geology of the Dinggye region

The Dinggye region is located in the central part of the Himalayan orogenic belt and the Makalu summit is within the south-western corner of the region (Fig. 2). Main litho-tectonic units in this region include the THS, GHC and Ama Drime Massif (ADM, Groppo et al. 2007; Jessup et al. 2008; Kali et al. 2010). The GHC in the Dinggye region is composed of two sub-units: (a) the Jiangdong group mainly consists of an upper-amphibolite- to granulite-facies migmatitic paragneiss (Borghi et al. 2003) that is rich in leucosome (Fig. 3a–d) and is locally crosscut by leucogranite

plutons or sills (Fig. 3e, f); (b) acting as a transitional zone from the GHC to the THS, the Rouqiechun group (Everest series) mainly consists of a lower-amphibolite-facies gneiss or schist and is rich in leucogranite and pegmatite sills (Figs. 2, 3g, h). Foliation of the GHC rocks mostly dips to the north or northwest at moderate angles (20°–50°) and lineation of its top portion (the STD shear zone) plunges to the northeast at 5°–30°. Monazite U–Th–Pb dating of the migmatitic paragneiss yields a complex pattern of ages from ~39–20 Ma (Liu et al. 2007; Cottle et al. 2009a). On the contrary, most of the leucogranite sills yield Miocene ages of 16–14 Ma (Cottle et al. 2009a; Leloup et al. 2010) with some

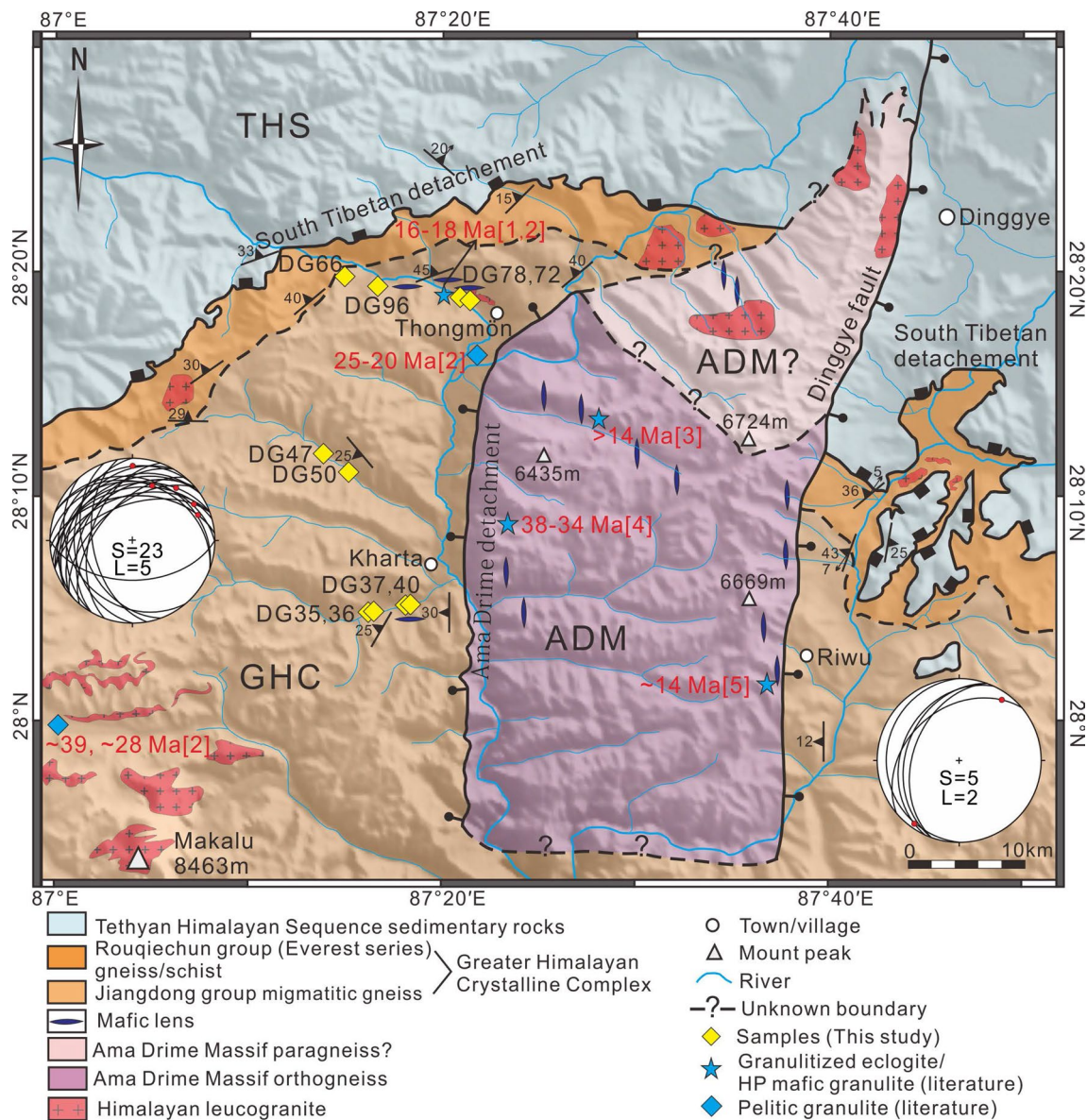


Fig. 2 Simplified geological map of the Dinggye region, southern Tibet. Location of the Dinggye region is available in Fig. 1. References: [1] Li et al. (2003), [2] Cottle et al. (2009a), [3] Cottle et al.

(2009b), [4] Kellett et al. (2014), [5] Wang et al. (2017). Projection: S, foliation; L, lineation

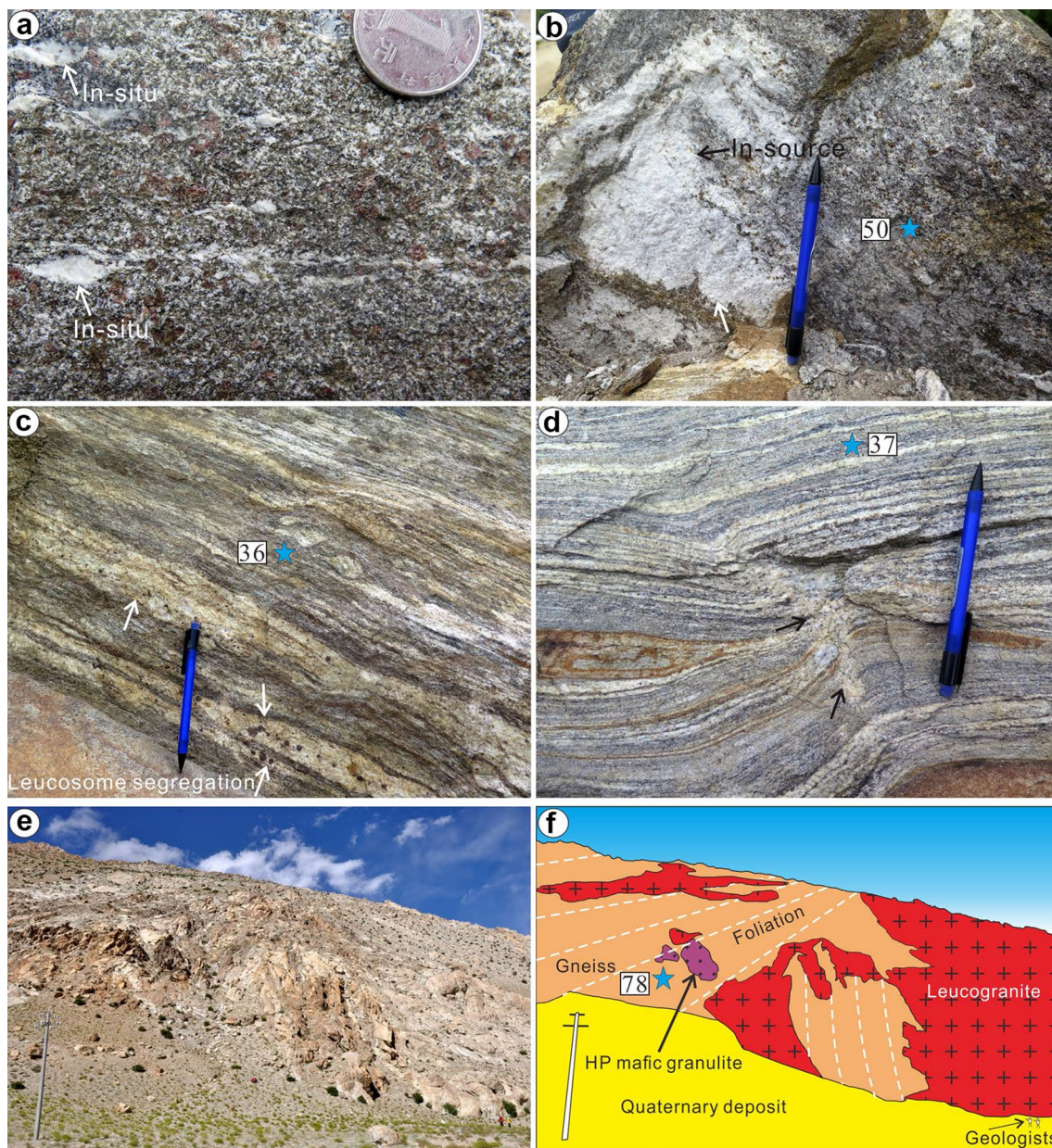


Fig. 3 Outcrop photographs of granulite-facies migmatites from the Jiangdong group of the Greater Himalayan Crystalline Complex (GHC) in the Dinggye region. **a** Garnet-bearing migmatitic metapelite with pockets of melt crystallized in situ within mesosome. **b** Garnet-bearing migmatitic metapelite. Melt forms segregations within the mesosome. **c** Garnet-bearing migmatitic metapelite. Melt segregations form cm-wide leucosome. Peritectic garnet is present within

the leucosome segregations. **d** Garnet-bearing migmatitic metapelite. Former melt is distributed to form a syn-anatectic flow structure. The arrows show small leucosome segregations that connect to form a wider vertical leucosome vein. **e, f** Metapelitic gneiss intruded by a leucogranite pluton that bended the foliation. A lens of high-pressure mafic granulite is visible in this outcrop. The stars show location of samples 15DG50, 36, 37 and 78

dates that are slightly older (~21 Ma, Cottle et al. 2009a). High-pressure mafic granulite lenses that consist of clinopyroxene-plagioclase symplectitic texture are enclosed in the Jiangdong group (Figs. 2, 3f), and metamorphic zircons in these rocks give U–Pb ages of ~18–16 Ma (Li et al. 2003; Cottle et al. 2009a). High-pressure mafic granulites were also identified to the south of the Dinggye region along the

Arun river valley (Fig. 1), and Corrie et al. (2010) proposed that these rocks underwent ‘eclogite-facies metamorphism’ at ~670 °C and ≥15 kbar at 23–16 Ma.

The ADM is a unique unit within the Himalayan chain and contains abundant Paleoproterozoic orthogneisses (~1.8 Ga, Cottle et al. 2009b) and granulitized eclogite lenses. According to the metamorphic grade, the ADM

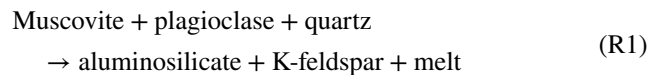
should be included into the GHC (Kali et al. 2010; Leloup et al. 2010), but stratigraphically the ADM has affinity with the LHS based on the ~1.8 Ga orthogneiss (Lombardo and Rolfo 2000; Groppo et al. 2007). In this study, we follow the classification of Jessup et al. (2008) and Cottle et al. (2009b) that refer to a separated ADM so as to avoid this debate. The eclogites in the ADM were overprinted by high-temperature granulite-facies metamorphism (4–10 kbar and >750 °C, Groppo et al. 2007) during exhumation, and preserved peak-stage minerals are clinopyroxene-plagioclase symplectite (Lombardo and Rolfo 2000; Groppo et al. 2007) or relict omphacite inclusions in garnet (Jd 28–22 wt%, Wang et al. 2017). The ADM rocks represent the deepest (50–70 km) buried Indian crustal rocks within the central part of the Himalayan orogenic belt. Zircon U–Pb dating of these granulitized eclogites yield ages of ~14 Ma, and there is debate whether these ages represent peak pressure (Wang et al. 2017) or the granulite-facies overprint (Cottle et al. 2009b; Kali et al. 2010). In contrast, Lu–Hf dating of the eclogite gives an age of 38–34 Ma (Kellett et al. 2014). Monazite Th–Pb ages of the country rock (orthogneiss) are ~13–12 Ma (Cottle et al. 2009b; Kali et al. 2010). Foliation of the ADM dips to the west at its west wing and to the east at its east wing, presenting an east–west trending extension (Kali et al. 2010). Kali et al. (2010) described the paragneiss sub-unit within the ADM as a metapelite that yield peak pressure of >15 kbar, higher than most other metapelites of the GHC. Doming and exhumation of the ADM has been related to the movement along the Xainza-Dinggye rift since ~13 Ma, which also marks the initiation of orogen-parallel extension (Zhang and Guo 2007; Jessup et al. 2008; Kali et al. 2010).

Sample description

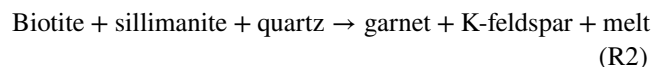
Nine metasedimentary samples and one leucogranite sample were collected from the Jiangdong group of the GHC (west wing, Kharta and Thongmön sections, Fig. 2). The localities, GPS coordinates, rock types, mineral assemblages and melting conditions are summarised in Table 1 and described below. Samples 15DG35, 36, 37, 40, 47, 50, 72, 78 and 66 were collected as migmatitic metapelite and metapsammite samples from the Jiangdong group. Leucosome segregations are widely distributed across the outcrops, exhibiting the evolution of melt formation, convergence and migration. In the mesosome portion, melt usually crystallizes in situ and forms strings of discrete lenses or centimetre-scale pods (Fig. 3a). In a few outcrops, larger leucosome pores can reach decimetre-scale (Fig. 3b). In most rocks, centimetre- to decimetre-scale leucosome layers are generally parallel to the foliation of the protolith rock (Fig. 3c, d). From the leucosome proportion within each outcrop it was estimated that in most localities the melt

volume was $25 \pm 5\%$; in sample 15DG66, a melt volume of $15 \pm 5\%$ was estimated. In the outcrop where sample 15DG78 was collected, migmatitic metapelites or metapsammites are intruded by leucogranite sills and the foliation is bent (Fig. 3e, f). Most samples used for petrology and geochronology were collected from the mesosome portion that contains small segregations of leucosome. Samples 15DG72 and 78 were collected from the country rock of a high-pressure mafic granulite lens (Li et al. 2003; Cottle et al. 2009a). Sample 15DG96 represents a two-mica leucogranite dikelet that intruded into the surrounding migmatitic metapelites in the GHC.

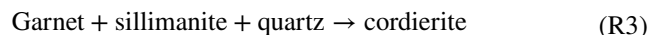
All the migmatitic metapelite samples are composed of an equilibrium mineral assemblage of garnet, sillimanite, plagioclase, K-feldspar, biotite, quartz and rutile or ilmenite (Fig. 4a–f). Kyanite is only preserved in sample 15DG50 in association with rutile, as relicts surrounded by plagioclase (Fig. 4a). Garnet porphyroblasts in the mesosome portion are generally anhedral and contain inclusions of plagioclase, biotite, rutile and quartz in the core or rim or polymineralic inclusions of muscovite, K-feldspar, plagioclase, biotite and quartz in the rim (Fig. 4c). Some plagioclase grains are rich in albite and orthoclase exsolutions. Muscovite is generally absent in the matrix of the mesosome portion. However, phase equilibria modelling of sample 15DG36 indicates presence of muscovite at prograde conditions and breakdown of muscovite approaching the pressure peak (Fig. 5a). Therefore, we infer that muscovite has been consumed by prograde dehydration-melting reactions such as (Le Breton and Thompson 1988).



A few tiny muscovite grains are present in the leucosome domain and are interpreted as back-reaction of melt + sillimanite + K-feldspar. In sample 15DG36, leucosome segregations contain quartz, K-feldspar, plagioclase and abundant euhedral garnet crystals (Fig. 3c), indicating the biotite dehydration-melting reaction (Spear et al. 1999)



In samples 15DG35, 36, 37 and 50, cordierite or cordierite-quartz pairs occur as corona replacing the rims of garnet porphyroblasts (Fig. 4e) following reaction (Hensen 1971)



These samples also contain green spinel, which is present either as tiny crystals in the cordierite corona or occurs as spinel-plagioclase symplectite replacing residual biotite (Fig. 4f) possibly by reactions (Clarke and Powell 1991; Ouzegane and Boumaza 1996)

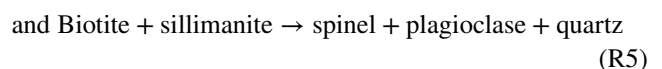
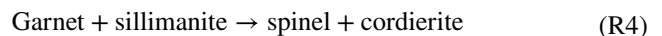


Table 1 Localities, mineral assemblages and P–T conditions of investigated samples from the GHC, Dinggye Himalaya

Sample	Locality	GPS coordinates	Rock type	M ₁	M ₂	M ₃	Melting volume	Melting reaction	GASP P (kbar)	GB T (°C)	Zr-in-rutile T (°C)
15DG36	Kharta	N28°04'16.80", E87°17'01.51"	Migmatitic metapelite	Ms, Rt, Pl, Qz	Grt (~12%), Sil, Pl, Bt, Kfs, Qz, Rt, Ilm	Crd, Spl + Pl	25 ± 5%	Ms/Bt dehydration	8.6 ± 0.8	791 ± 25	803 ± 14
15DG66	Thongmön	N28°20'19.06", E87°15'23.15"	Migmatitic metapsammite		Grt (~2%), Pl, Bt, Kfs, Qz, Rt, Ilm		15 ± 5%	Ms/Bt dehydration			760 ± 17 ^b
15DG37	Kharta	N28°04'51.57", E87°18'56.18"	Migmatitic metapelite		Grt (~7%), Sil, Pl, Bt, Kfs, Qz, Rt, Ilm	Crd, Spl + Pl	25 ± 5%	Ms/Bt dehydration	9.7 ± 0.8	742 ± 25	822 ± 16
15DG35	Kharta	N28°04'16.80", E87°17'01.51"	Migmatitic metapelite		Grt (~1%), Sil, Pl, Bt, Kfs, Qz, Rt, Ilm	Crd, Spl + Pl	25 ± 5%	Ms/Bt dehydration			802 ± 17 ^b
15DG47	Kharta	N28°11'25.21", E87°14'44.48"	Migmatitic metapelite		Grt (~5%), Sil, Pl, Bt, Kfs, Qz, Rt, Ilm		25 ± 5%	Ms/Bt dehydration	5.3 ± 0.8	746 ± 25	
15DG50	Kharta	N28°10'58.79", E87°15'54.46"	Migmatitic metapelite	Ky, Rt	Grt (~14%), Sil, Pl, Bt, Kfs, Qz, Rt, Ilm	Crd, Spl + Pl	25 ± 5%	Ms/Bt dehydration	5.9 ± 0.8	757 ± 25	780 ± 16
15DG40	Kharta	N28°04'51.57", E87°18'56.18"	Migmatitic metapelite		Grt (~17%), Pl, Bt, Kfs, Qz, Rt, Ilm		20 ± 5%	Ms/Bt dehydration	6.9 ± 1.2 ^a	835 ± 50	
15DG72	Thongmön	N28°19'30.31", E87°19'32.46"	Migmatitic metapelite		Grt (~4%), Bt, Kfs, Pl, Sil, Qz, Rt, Ilm		25 ± 5%	Ms/Bt dehydration	5.4 ± 0.8	757 ± 25	
15DG78	Thongmön	N28°19'05.43", E87°21'23.72"	Migmatitic metapelite		Grt (~1%), Bt, Kfs, Pl, Sil, Qz, Rt, Ilm		25 ± 5%	Ms/Bt dehydration			790 ± 14 ^b
15DG96	Thongmön	N28°19'22.82", E87°17'31.78"	Leucogranite		Pl, Kfs, Bt, Ms, Qz		/	/			

Degree of partial melting was defined by textures and amount of leucosome in the samples. Zr-in-rutile temperatures were calculated using the thermometer of Tomkins et al. (2007)

^a Calculated by GBPQ barometer of Wu et al. (2004)

^b Calculated using pressure estimates of adjacent samples

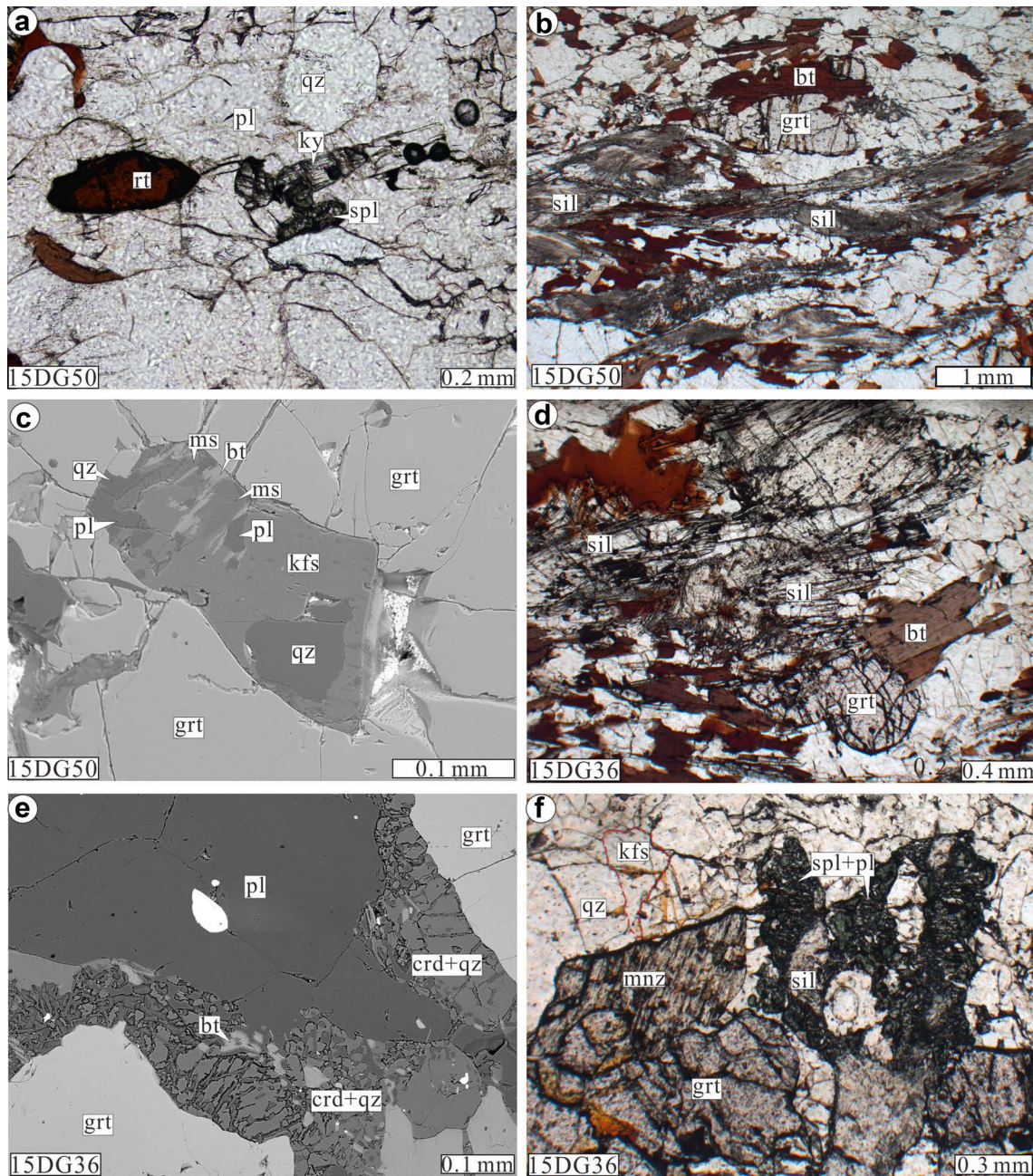


Fig. 4 Photomicrographs of thin sections of investigated samples. **a** Relict kyanite and rutile crystals preserved within a plagioclase grain. **b** Typical sillimanite-grade mineral assemblage composed of anhedronal garnet, plagioclase, quartz and abundant fibrolite or prismatic sillimanite aligned with biotite. Muscovite is absent. **c** Polymineralic inclusions of muscovite, biotite, plagioclase, K-feldspar and quartz in a garnet porphyroblast (BSE image). **d** Typical sillimanite-grade min-

eral assemblage composed of large prismatic sillimanite and biotite. **e** Cordierite + quartz forming a corona around garnet (BSE image). **f** A large monazite crystal coexists with garnet and quartz. A large spinel + plagioclase symplectite grows over prismatic sillimanite and garnet. Mineral abbreviations are according to Whitney and Evans (2010)

Migmatitic metapsammite samples 15DG66 and 40 consist of a similar mineral assemblage as the migmatitic metapelite, but sillimanite is absent.

Analytical methods

All analyses were performed at the Institute of Geology and Geophysics, Chinese Academy of Sciences (IGGCAS),

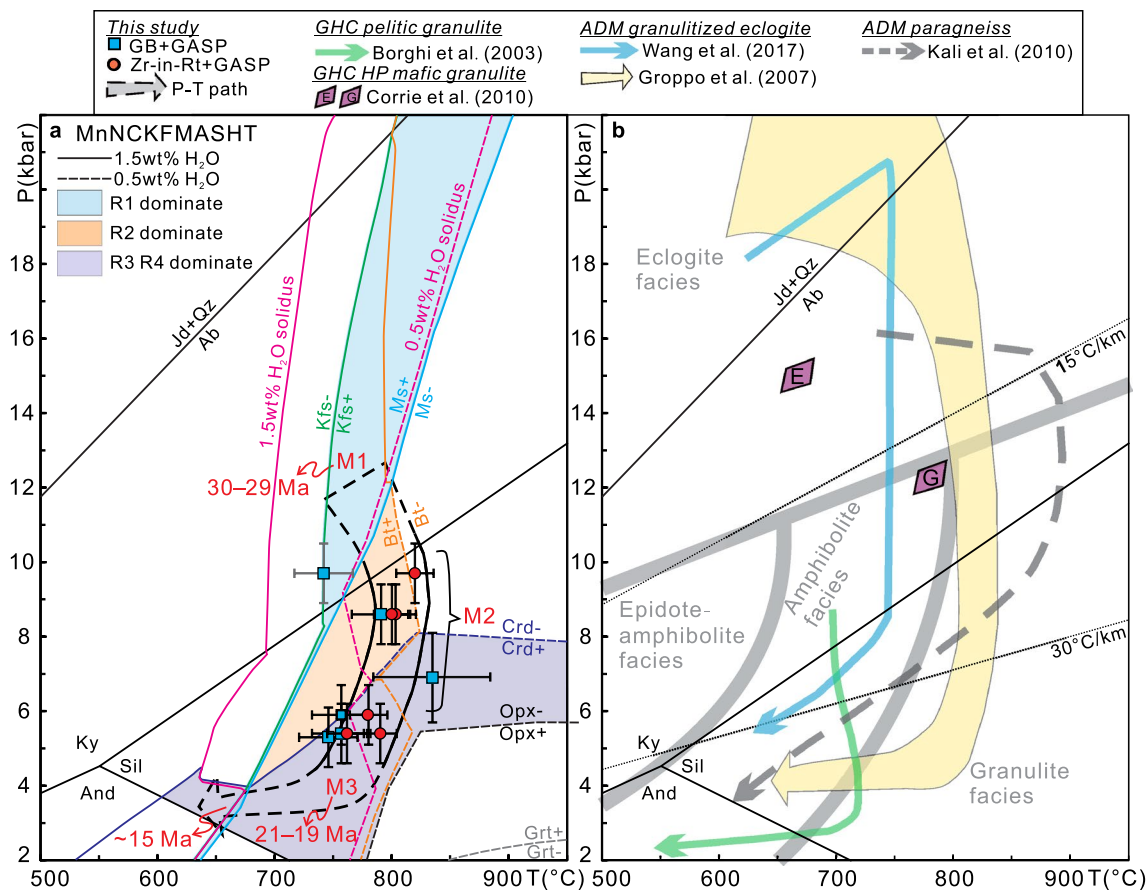


Fig. 5 **a** P–T results from thermobarometers plotted in the phase diagram calculated using the bulk composition of sample 15DG36 measured by X-ray fluorescence spectrometer. Solid and dashed lines indicate phase boundaries using H₂O contents of 1.5 wt% and 0.5 wt%, respectively. An H₂O content of 1.5 wt% is close to what needed to saturate the metapelite and is used to predict the prograde conditions. An H₂O content of 0.5 wt% is close to the conditions when the sam-

ple crystallized after melt extraction/loss and is used to model the decompression/retrograde conditions. See Online Resource Fig. S1 for detailed method and bulk compositions used. **b** P–T–time paths from the literatures. **e** and **g** represent minimum 'eclogite-facies' and high-pressure granulite-facies metamorphic conditions, respectively, from Corrie et al. (2010). ADM Ama Drime Massif

Beijing. Nine metapelitic and metapsammitic samples from the Dingye area were selected for mineral chemical composition and U–Th–Pb analyses whereas one leucogranite sample was selected for U–Th–Pb analyses. Chemical compositions of the minerals (Online Resource Tables S1–3) were determined using a JEOL JXA-8100 electron microprobe. The working conditions were set to 15 kV accelerating voltage, a 20 nA beam current and a beam diameter of 2–5 μ m. Back-scattered electron (BSE) and cathode-luminescence (CL) images were produced with a Nova Nano 450 scanning electron microscope (SEM).

Monazite, zircon and rutile crystals were separated using standard heavy liquid and magnetic technique, and hand-picked under a binocular microscope. The grains were then mounted in epoxy resin and polished to expose the grain centres. Inclusions in monazite and zircon were identified by an Oxford Aztec Energy Dispersive X-ray system installed on the SEM. Transmitted- and reflected-light microscopic

images of monazite and zircon were also used to avoid inclusions and fractures during analysis. Yttrium (Y), Th and U compositional mapping of the monazite grains was performed using a CAMECA SXFiveFE electron microprobe under the analytical condition of 15 kV accelerating voltage, ~200 nA beam current, 50–100 ms dwell times and pixel step sizes of 0.2–0.5 μ m.

U–Th–Pb analyses

U–Th–Pb analyses of monazite were performed at IGGCAS with an Agilent 7500a quadrupole–inductively coupled plasma–mass spectrometry (Q-ICP-MS), which was coupled with a pulsed 193 nm excimer laser ablation system. A 50–100 mJ energy at a repetition rate of 4 Hz and a small spot size of ~24 μ m were used during the analyses. Each analysis measures the background for 20–25 s before switching on the laser for 45–50 s. Reference material was

analysed each fifth analysis. The measured $^{206}\text{Pb}/^{238}\text{U}$ and $^{208}\text{Pb}/^{232}\text{Th}$ ratios were corrected using reference monazite Delaware 44069 (425 Ma, Aleinikoff et al. 2006). Accuracy and precision of the analyses were evaluated with a secondary reference monazite Jefferson County (Th–Pb age 359 ± 2 Ma, mean square of weighted deviates (MSWD) 0.5, $N = 77$) or E0013 (Th–Pb age 594 ± 6 Ma, MSWD 1.5, $N = 15$), which are identical within errors with the recommended values (Jefferson County $^{207}\text{Pb}/^{235}\text{U}$ age by isotope dilution thermal ionization mass spectrometry (ID-TIMS), 360 ± 1 Ma, Peterman et al. 2012; E0013 $^{207}\text{Pb}/^{235}\text{U}$ age 587 ± 5 Ma by ID-TIMS, Janasi et al. 2003). Data reduction, including corrections for baseline, instrumental drift, mass bias and downhole fractionation were calculated using GLITTER 4.4. Uncertainties of the corrected $^{206}\text{Pb}/^{238}\text{U}$ and $^{208}\text{Pb}/^{232}\text{Th}$ ratios are quoted at the 2σ or 95% confidence level. U–Th–Pb data are listed in Online Resource Tables S4, S5, S8.

Measurements of U, Th and Pb isotopes of zircon were performed using the Cameca IMS 1280 secondary ion mass spectroscopy (SIMS) at IGGCAS. Instrumental conditions and data acquisition were generally as described in Li et al. (2009). The data were collected in sets of seven scans throughout the masses with a primary O^{2-} ion beam spot of $20 \times 30 \mu\text{m}$ and reference material was analysed each third analysis. The measured $^{206}\text{Pb}/^{238}\text{U}$ ratio was corrected using reference zircon Plésovice ($^{206}\text{Pb}/^{238}\text{U}$ age 337 Ma, Sláma et al. 2008). U and Th concentrations were calibrated against zircon standard Harvard 91500 (Th = 29 ppm, and U = 81 ppm, Wiedenbeck et al. 1995). To monitor the external uncertainties, an in-house zircon standard Qinghu was alternately analysed as an unknown together. Eight measurements on Qinghu zircon yield a Concordia age of 160 ± 2 Ma (MSWD 0.1, $N = 8$), which is identical within error with the recommended value of 159.5 ± 0.2 Ma (Li et al. 2013). A long-term uncertainty of 1.5% (1σ RSD) for $^{206}\text{Pb}/^{238}\text{U}$ measurements of the standard zircons was propagated to the unknowns (Li et al. 2010), despite that the measured $^{206}\text{Pb}/^{238}\text{U}$ error in a specific session is generally $\leq 1\%$ (1σ RSD). For the analyses yielding Cenozoic ages, the data were corrected for common Pb based on the measured $^{207}\text{Pb}/^{206}\text{Pb}$ (by assuming concordance), while the pre-Cenozoic inherited ages were corrected using the measured ^{204}Pb (Williams 1998). Corrections are sufficiently small to be insensitive to the choice of common Pb composition, and an average of present-day crustal composition (Stacey and Kramers 1975) is used for the common Pb. Data reduction and age calculation was carried out using the software Isoplot/Ex v3.7 (Ludwig 2008) and the ^{238}U , ^{235}U , and ^{232}Th decay constants of Steiger and Jäger (1977) were used. Average U–Pb ages are quoted at 95% confidence level. Analytical U–Th–Pb data are listed in Online Resource Tables S6, S8.

Mineral trace elements analyses

Trace elements analyses of monazite, zircon and rutile were obtained with the LA-Q-ICP-MS at IGGCAS. Trace elements of monazite were obtained simultaneously during the U–Th–Pb analyses, whereas those of zircon were performed on the same site of the $2\text{-}\mu\text{m}$ -deep SIMS pits. Spot sizes of $24 \mu\text{m}$ (monazite), $32 \mu\text{m}$ (zircon) and $48 \mu\text{m}$ (rutile) were used and reference material was analysed each tenth analysis. External calibration was performed relative to NIST 610 glass using the values recommended by Pearce et al. (1997) and internal standardization was based on stoichiometry of Ce in monazite (23.6 wt%), Ti in rutile (59.93 wt%) and Si in zircon (16.25 wt%). Accuracy and precision of the analyses were evaluated with a BCR-2G secondary glass standard and are always better than 10% combined. Analyses that have apparent contamination from inclusions or those with insufficient data-collecting duration (<10 s) were discarded. For rutile analyses, the $48\text{-}\mu\text{m}$ laser pit was always located at the centre of the grains to avoid possible complications from Zr diffusion at the rim during cooling. Trace elements data reduction was performed using the software Glitter 4.4. Rare earth element (REE) patterns of monazite and zircon were normalized to chondrite (McDonough and Sun 1995). Analytical data are listed in Online Resource Tables S4–7.

Thermobarometry

Conventional thermobarometry

Garnet porphyroblasts in the studied samples have components of almandine (63–77%), spessartine (1–5%), pyrope (15–28%) and grossularite (2–11%) (Online Resource Table S1). In general, garnet porphyroblasts in most samples have relatively flat zoning patterns. In a single garnet porphyroblast, X_{spss} , and X_{Fe} ($X_{\text{Fe}} = \text{Fe}/(\text{Fe} + \text{Mg})$) are usually flat from core to mantle (near-rim). However, weak resorption could be observed at the rim (or outmost rim) with slight increase in X_{spss} and X_{Fe} , and decrease in X_{prp} , which was probably caused by diffusion during cooling. Therefore, for thermobarometric calculations, garnet mantle or near-rim compositions were used for most samples. In each sample, different biotite grains in the matrix have relatively homogeneous compositions or show no chemical zoning within grain. X_{Mg} in the biotite has a small range of 0.43–0.53. Plagioclases in the matrix usually have flat or quite weak zoning and compositions between different grains show no large variation. Plagioclase grains that are in contact with garnet have similar or relatively higher anorthite (An) components compared to the matrix grains. Average An values of matrix plagioclase grains in

each sample range of 0.20–0.36. Average compositions of matrix biotite and plagioclase were used for thermobarometric calculations.

The garnet–biotite (GB) thermometer (Holdaway 2000) and the garnet– Al_2SiO_5 –quartz–plagioclase (GAPQ) barometer (Holdaway 2001) or garnet–biotite–plagioclase–quartz (GBPQ) barometer (Wu et al. 2004) was used for P–T calculation. The Fe^{2+} components in garnet and biotite calculated from the AX software were used for calculation. The recommended errors are ± 0.8 kbar, 25 °C for GB–GASP (Holdaway 2001) and ± 1.2 kbar, 50 °C for GB–GBPQ (Wu et al. 2004). The calculated P–T results are the recorded maximum temperatures and corresponding equilibrium pressures instead of peak pressures. The calculated results and uncertainties are listed in Table 1, and plotted in the P–T diagram (Fig. 5). The estimates show that metamorphic temperatures of most studied samples are in the range $740\text{--}790 \pm 50$ °C (rounded to 10 °C), whereas sample 15DG40 yields higher metamorphic temperature of ~ 830 °C although it was collected close to samples 15DG35, 36 and 37. The corresponding equilibrium pressures have a relatively large variation of 5–10 kbar (rounded to 1 kbar). Most of the calculated P–T results were plotted within the granulite-facies range except that of sample 15DG37, which recorded the highest pressure condition.

Zr-in-rutile thermometer

Zr-in-rutile temperatures were calculated using the calibration of Tomkins et al. (2007) for the β -quartz field and the pressure estimates from the GASP or GBPQ barometer were used for correction. Generally, differences of temperature results using different calibrations (e.g., Watson et al. 2006; Ferry and Watson 2007) are less than ± 30 °C. Uncertainties are calculated by considering a conservative analytical error of $\pm 15\%$ in zirconium measurements, ± 0.8 or ± 1.2 kbar for pressure estimates and a $\pm 3\%$ (± 20 °C) propagated uncertainty from the calibration of the thermometer. The activity of Si and Zr is fully buffered, because all the studied samples are rich in quartz and zircon. Rutile grains in the studied samples are relatively clear and homogeneous in BSE images. The brachyaxis of most rutile grains are 80–150 μm in radius. Analyses that showed high concentrations of Si, Zr, Hf, Fe, or Th were considered contaminated by possible inclusions of zircon, monazite or ilmenite and were discarded. The studied samples generally have a zirconium content of 1000–2000 ppm, and the calculated Zr-in-rutile average temperatures are $760\text{--}820 \pm 20$ °C (Table 1). The Zr-in-rutile temperatures are slightly higher than that what obtained with the garnet–biotite thermometer.

Geochronology and trace elements

Internal zoning of monazite is described according to the high-contrast BSE images or Y and Th elements maps, whereas zircon is described according to the CL images. Average $^{208}\text{Pb}/^{232}\text{Th}$ or $^{206}\text{Pb}/^{238}\text{U}$ ages are reported according to the statistically consistent groups ($n \geq 5$). For most weighted mean ages, the MSWD is below the threshold of 2.5; otherwise, a range of dates is reported. For Th-rich minerals such as monazite, excess ^{206}Pb due to decay of ^{230}Th can lead to overestimate the real age especially for young ages (Schärer 1984). Therefore, monazite Th–Pb ages are regarded as more accurate than U–Pb ages, and the weighted mean Th–Pb ages were calculated for each sample unless otherwise stated. Inclusions in monazite and zircon were checked by Energy Dispersive X-ray and Raman spectroscopy. Monazite and zircon ages, trace element signatures and inclusions are summarised in Table 2.

Monazite U–Th–Pb dating (grain separates)

Monazite age results in the studied samples are complex and samples that have similar ages are described together. In metapelitic sample 15DG36, most monazites are unzoned and a few grains contain a core–rim structure (Fig. 6a). The cores and most unzoned grains yield a statically consistent cluster of Th–Pb ages at 29.0 ± 0.3 Ma (MSWD 1.1, N 26/26). The rims and other unzoned grains have scattered ages of 27–20 Ma (N = 13). Chemically, the Y and heavy rare earth elements (HREE) contents of the older and younger domains overlap (Y 1000–6000 ppm, $\text{Gd}_\text{N}/\text{Yb}_\text{N}$ 100–900, Fig. 7a). The negative Eu anomaly in the REE pattern shows a general increasing trend from older to younger domains (Eu/Eu^* 0.47–0.17, Online Resource Fig. S2a).

In samples 15DG66, 37, 47 and 50, monazite grains usually consist of BSE-bright cores and BSE-grey rims or are unzoned, whereas grains in sample 15DG35 consist of BSE-dark inherited cores and BSE-grey Miocene rims (Fig. 6b–f). Monazite in the metapsammitic sample 15DG66 is slightly older with cores defining an age of 24.9 ± 0.4 Ma (MSWD 0.5, N 10/10, Fig. 6b) and rims defining an age of 23.9 ± 0.3 Ma (MSWD 1.8, N 30/32), even though individual core and rim ages partly overlap. Cores generally have lower Y and HREE contents (Y 700–2000 ppm, $\text{Gd}_\text{N}/\text{Yb}_\text{N}$ 350–1100) than rims or unzoned grains (Y 1000–16,000 ppm, $\text{Gd}_\text{N}/\text{Yb}_\text{N}$ 50–700, Fig. 7b), and the negative Eu anomaly increases from cores to rims or unzoned grains (Eu/Eu^* 0.14–0.03). Dates of the metapelitic sample 15DG37 present a larger scatter between 22 and 17 Ma. Y content (Online Resource Fig. S2b) and negative Eu anomaly increase (Eu/Eu^* 0.31–0.03, Fig. 7c) from cores to rims (or unzoned grains), whereas the HREE content remains constant. The other three metapelitic samples

Table 2 Monazite and zircon ages, trace elements and index mineral inclusions of investigated samples from the GHC, Dinggye Himalaya

Sample	Monazite age (Ma)	Monazite Y (ppm)	Monazite Gd_N/Yb_N	Monazite Eu_N/Eu^*_N	Inclusions in monazite	Zircon age (Ma)
15DG36 (grain separates)	Cores + unzoned 29.0 ± 0.3 Ma, rims + unzoned 27–20 Ma	1000–6000	100–900	0.47 decrease to 0.17	Kfs–Qz + Ms (~30 Ma domain)	Cores 2524–818 Ma, mantles 29.7 ± 0.5 Ma, rims 20.7 ± 0.4 Ma
15DG36 (thin sections)	30.2 ± 0.2 Ma, 28–22 Ma, 20.8 ± 0.2 Ma	1500–11000	100–800	0.45 decrease to 0.18		
15DG66	Cores 24.9 ± 0.4 Ma, rims + unzoned 23.9 ± 0.3 Ma	Older 700–2000; younger 1000–16000	Older 350–1100; younger 50–700	0.14 decrease to 0.03	Kfs–Qz–Pl–Ms	
15DG37	Cores 22.3 ± 0.3 Ma, rims + unzoned 22–17 Ma	1200 increase to 16900	Older 50–750; younger 50–600	0.31 decrease to 0.03	Kfs–Pl–Ms–Bt	
15DG35	Cores 490–420 Ma, rims 19.6 ± 0.3 Ma	5300–11500	150–350	0.09–0.03	Kfs–Pl–Qz + Sil (abundant)	
15DG47	Cores 490–430 Ma, rims + unzoned 19.3 ± 0.2 Ma	4200–10700	50–350	0.10–0.05	Sil + Kfs–Qz–Pl–Ms	
15DG50	Cores + rims + unzoned 19.6 ± 0.2 Ma	1600–10100	50–350	0.24–0.05	Sil + Kfs	
15DG40	Unzoned 15.3 ± 0.2 Ma	400–5700	200–1000	0.16–0.07	Kfs	Cores 27–16 Ma, rims + unzoned 15.2 ± 0.2 Ma
15DG72	Cores 470–410 Ma, unzoned 14.9 ± 0.2 Ma	12000–30000	20–150	0.40–0.21	Sil (abundant) + Kfs–Qz–Pl	
15DG78	Cores 546–400 Ma, rims + unzoned 14.8 ± 0.2 Ma	8000–20400	50–250	0.27–0.08	Sil + Kfs–Qz–Ms	
15DG96	Unzoned 13.9 ± 0.2 Ma	5000–32000	20–150	0.12–0.05	/	

15DG35, 47, and 50 give similar weighted mean ages at ~20 Ma. One rim analysis in sample 15DG47 yield an older date of 26.9 ± 0.5 Ma. These ~20 Ma dates have similar Y contents and HREE patterns (Y 1600–11,500 ppm, Gd_N/Yb_N 50–350), and medium to strong negative Eu anomaly (Eu/Eu* 0.24–0.03, Fig. 7d–f).

Monazite grains in metapelitic samples 15DG40, 72, 78 and leucogranite sample 15DG96 are generally unzoned and yield similar weighted mean ages at ~15–14 Ma (Fig. 6g–k). Monazite uranium concentrations in sample 15DG40 are much lower (most 100–500 ppm) than metamorphic monazite in all other samples (most 2000–10,000 ppm). The U–Pb dates of the low-U monazite are older than the Th–Pb dates (Fig. 6g), suggesting that excess ^{206}Pb is more significant in the low-U monazite. A few monazite grains in sample 15DG78 present a core-rim structure and the rims yield similar ages as the unzoned grains. Chemically, monazite grains have low Y and HREE contents in sample 15DG40 (Y 400–5700 ppm, Gd_N/Yb_N 200–1000), high Y and HREE

contents in sample 15DG72, 15DG78 and 15DG96 (Y 8000–30,000 ppm, Gd_N/Yb_N 20–250), and medium to strong negative Eu anomaly in all samples (Eu/Eu* 0.35–0.07, Fig. 7g–k).

Besides the Cenozoic ages, in metapelitic samples 15DG35, 47, 72 and 78, some monazite grains consists of inherited core that yield ages of 500–400 Ma (Fig. 6m–p). A few rims or small cores that are not large enough to accommodate a laser beam yield intermediate dates of 400–40 Ma. Chemically, the inherited cores usually have high Y and HREE contents (Y 5000–24,000 ppm, Gd_N/Yb_N 20–150), and medium to strong negative Eu anomaly (Eu/Eu* 0.5–0.1, Fig. 7e, j, k).

Numerous mineral inclusions were observed in the Cenozoic-dated monazite (Fig. 8, Table 2). Minerals such as garnet, biotite, plagioclase, quartz and apatite were found as inclusions, and because these phases were present throughout the P–T trajectory, they are not indicative for specific metamorphic stages. Polymineralic inclusions

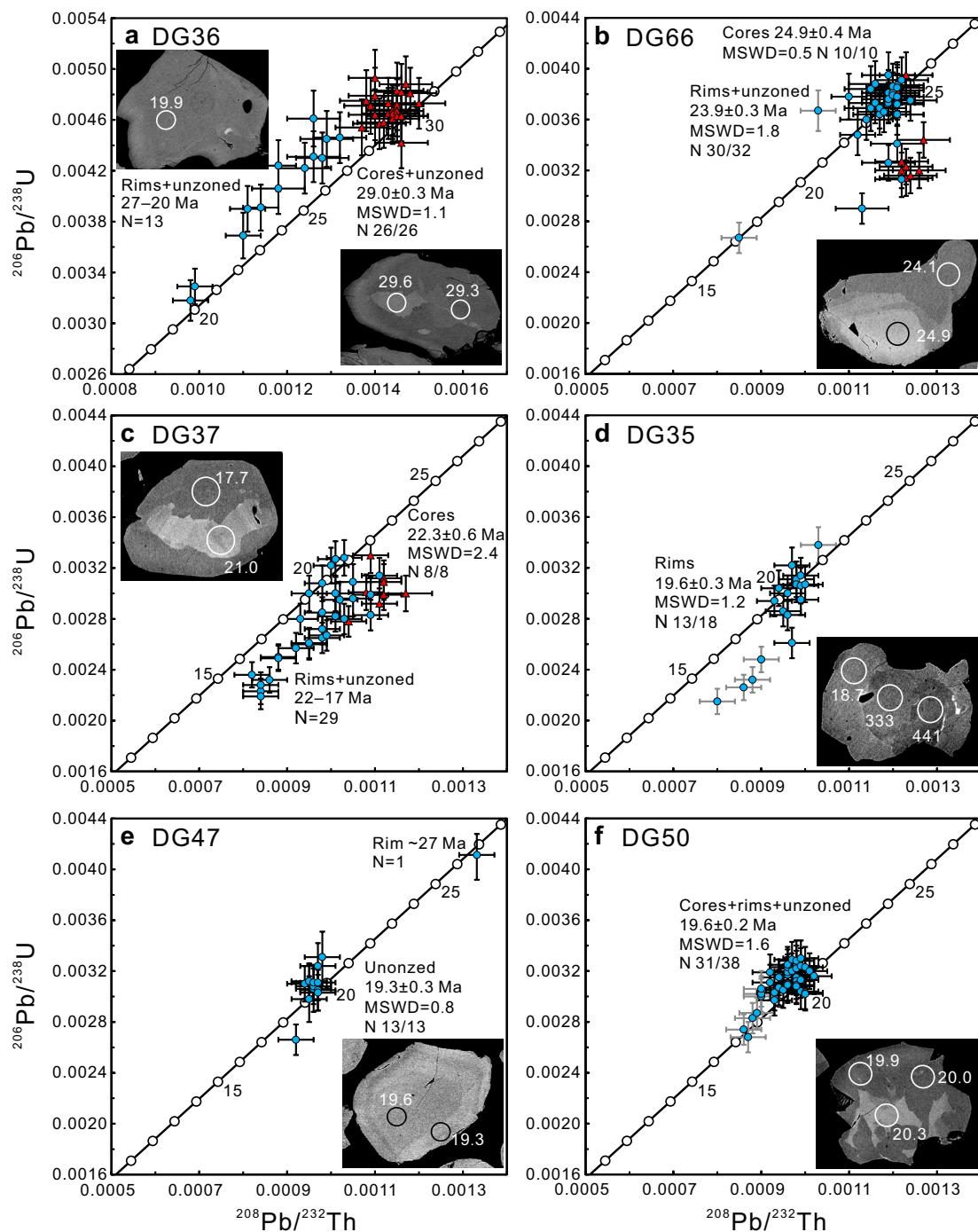


Fig. 6 $^{208}\text{Pb}/^{232}\text{Th}$ versus $^{206}\text{Pb}/^{238}\text{U}$ concordia plots of monazite age data from investigated samples. Representative BSE images of selected monazite crystals are also shown. Circles in the BSE images indicate the location of the laser pit and are ~24 μm in diameter, and

the numbers indicate $^{208}\text{Pb}/^{232}\text{Th}$ ages in Ma. Weighted mean ages are calculated from $^{208}\text{Pb}/^{232}\text{Th}$ ages. Crosses represent 2σ errors. Grey crosses are data excluded from weighted mean age calculation

of K-feldspar + quartz \pm plagioclase \pm muscovite were observed in monazite domains with ages of ~30 Ma (sample 15DG36), ~25–24 Ma (sample 15DG66), ~20 Ma (samples 15DG35, 37 and 47) and ~15 Ma (samples 15DG72 and 78). Some of these polyminerally inclusions have negative

crystal shapes (Fig. 8a, b) or are rounded (Fig. 8c, e, k). Abundant sillimanite inclusions are present in the younger (~20 and ~15 Ma) monazite domains of samples 15DG35, 47, 50, 72 and 78, but are absent in the domains with ~30 or ~25–24 Ma dates.

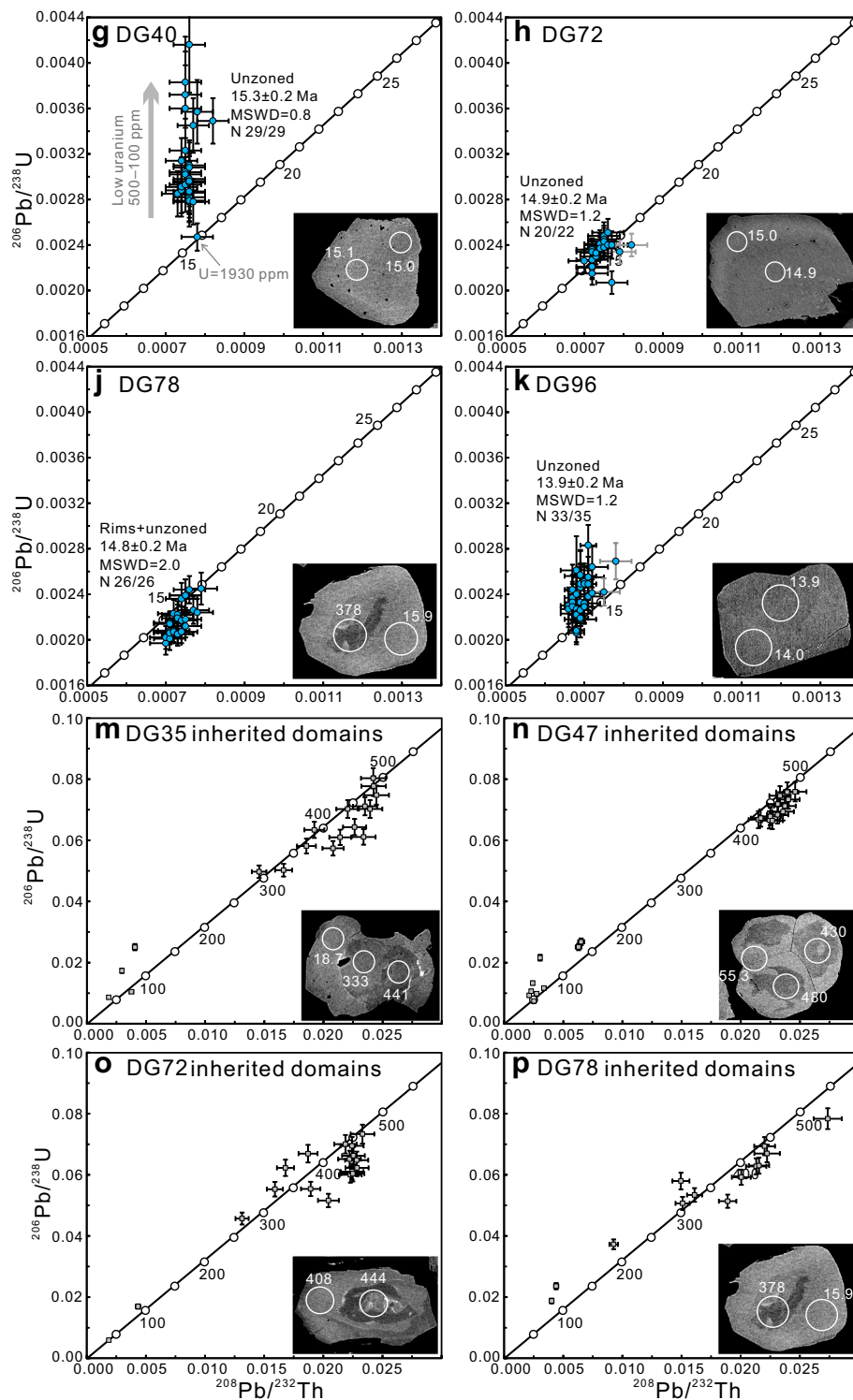


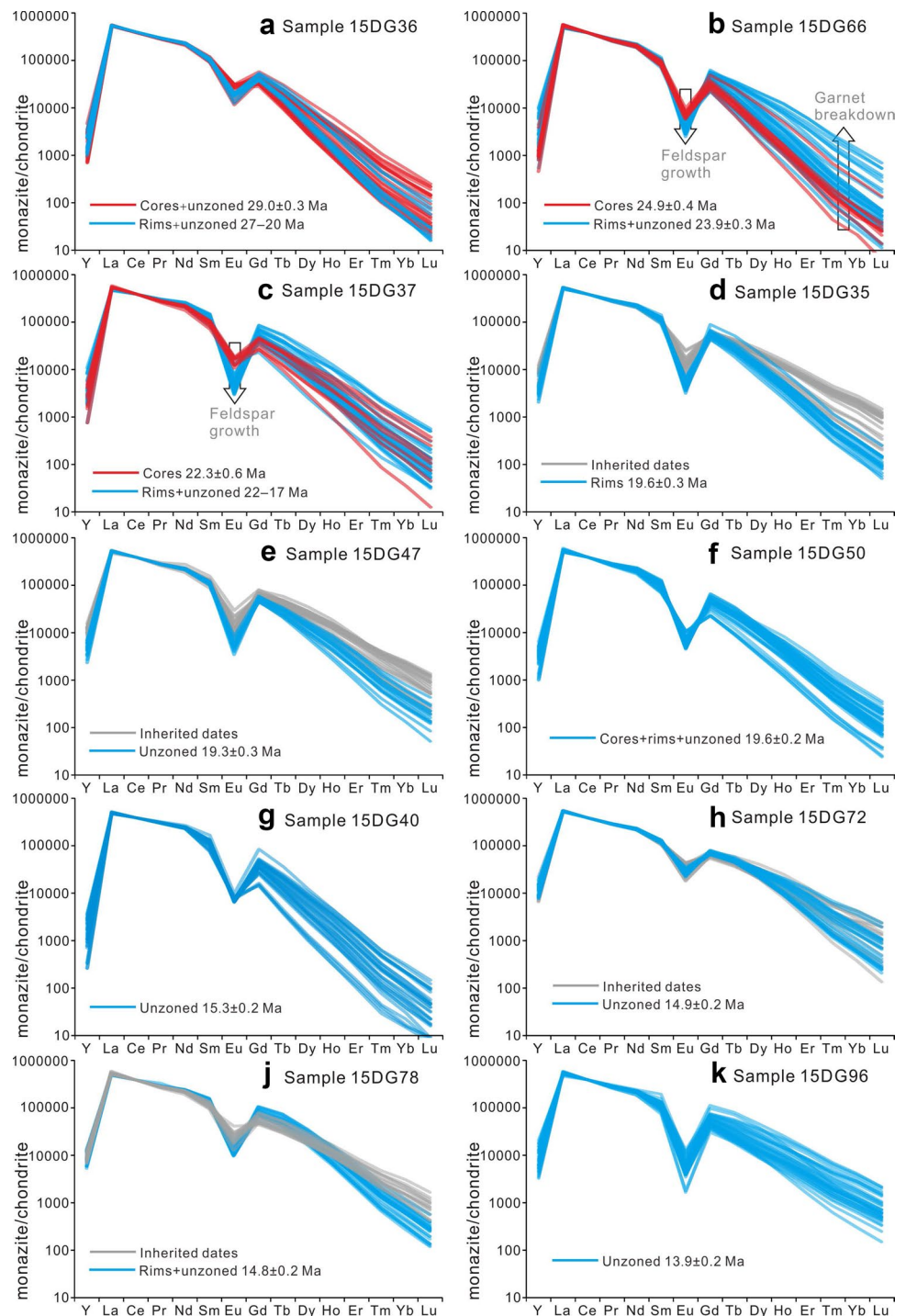
Fig. 6 (continued)

Monazite U–Th–Pb dating (in thin sections)

Monazites in sample 15DG36, which yield the oldest metamorphic ages in this study, were further dated in thin

sections to better correlate ages with textural positions. Y content of monazite is often a key discriminator for temporally distinct growth zones, and provides information to link monazite growth/crystallization events to other Y-bearing

Fig. 7 Chondrite-normalized Y and REE patterns for the dated monazites. The *arrows* highlight changes in HREE and Eu between different growth zones. Normalizing values are from McDonough and Sun (1995)



minerals such as garnet (Foster et al. 2000; Kohn et al. 2005; Rubatto et al. 2006). Therefore, representative monazite grains with different textural positions were selected for Y, Th and U compositional mapping using an EPMA before dating. 102 analyses were performed on 41 monazite grains from four thin sections of sample 15DG36.

Monazite 36Q2_mnz09 is a large ($\sim 350 \times 1000 \mu\text{m}$, Fig. 9a) anhedral grain encircled by garnet and quartz. The

monazite grain lacks significant BSE zoning, but shows patchy zoning in the Y and Th compositional maps, even if the two elements do not correlate. Y content is higher in the left or top-central portion, and decreases toward the right-bottom portion. Th–Pb ages are mostly around 31–28 Ma across domains with different Y contents. A few analyses located at the grain rim or within the core along fractures give significantly younger dates of 27–22 Ma. Monazite

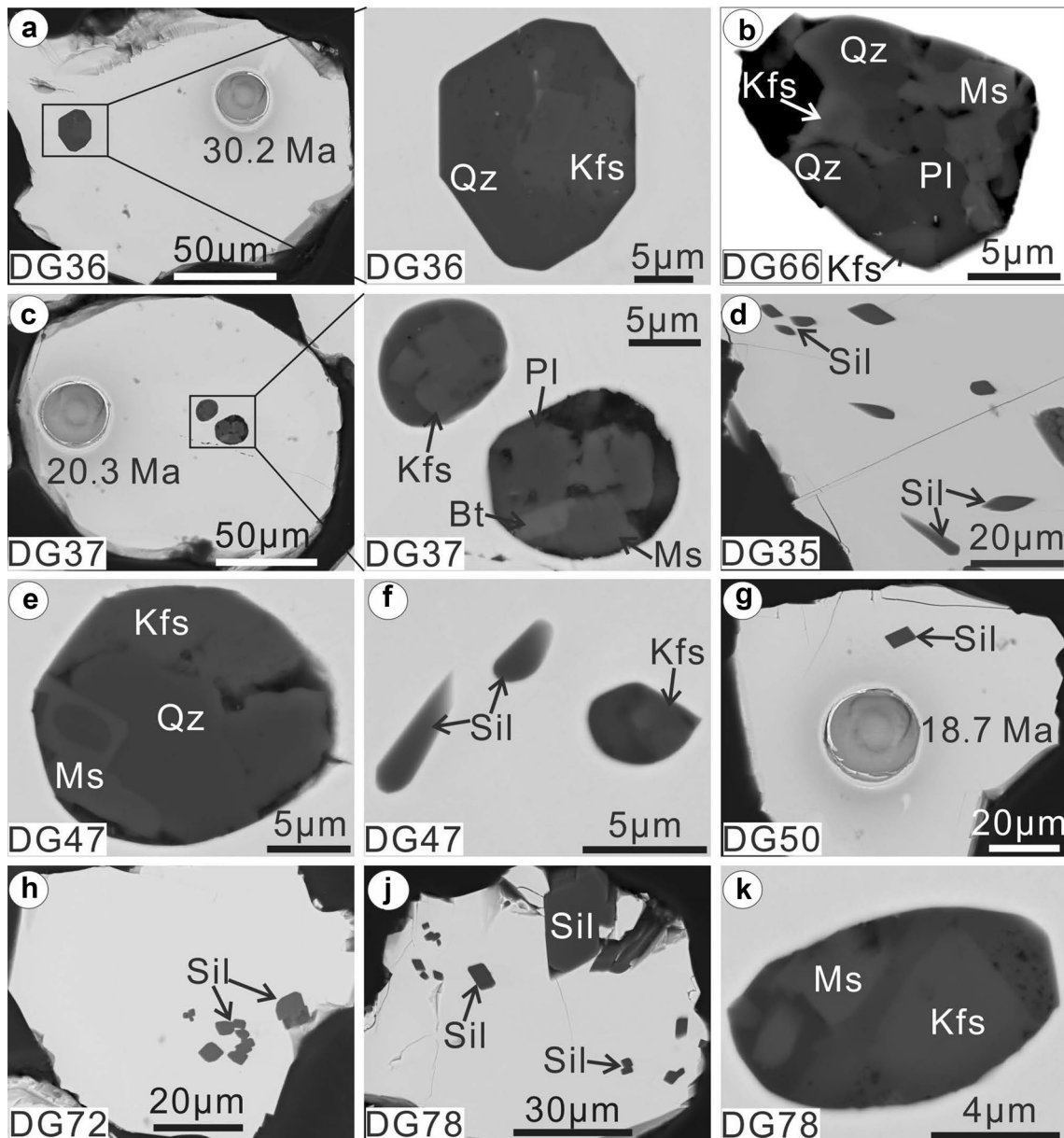


Fig. 8 Representative BSE images of mineral inclusions in monazite. *Holes* are the laser pit with $^{208}\text{Pb}/^{232}\text{Th}$ age given in Ma

36-1_mnz15 is medium in size ($150 \times 200 \mu\text{m}$), anhedral and included in biotite (Fig. 9b). It shows patchy zoning in BSE, whereas Y content is slightly higher in the centre, decreases toward the rim and reaches the highest value at the narrow outmost rim ($<10 \mu\text{m}$). Th displays roughly an opposite trend than Y. Ages obtained from this grain are mainly in the range 30–29 Ma, with two spots having slightly younger dates of ~ 27 Ma. Monazite 36-2_mnz06 is elongated and large in size ($200 \times 500 \mu\text{m}$, Fig. 9c). This monazite is surrounded by biotite and quartz grains, and shows a patchy zoning in BSE that correlates with Th content. Y is generally higher in the centre of the grain, and decreases toward the

rim. Dates from this grain are mainly in the range 30–28 Ma, with three analyses from the outermost rim giving younger dates of 25–22 Ma. Monazite 36-2_mnz08 is euhedral, medium in size ($150 \times 200 \mu\text{m}$) and included in cordierite (Fig. 9d). This grain lacks any zoning in BSE and Y compositional map with the exception of a narrow outmost rim ($<5 \mu\text{m}$) that is richer in Y. Th content shows only weak zoning. Four analyses from this grain yield dates of ~ 21 Ma.

Dating of monazite in thin sections yielded similar ages as grain separates. An older cluster of Th–Pb ages is defined at 30.2 ± 0.2 Ma (MSWD 2.4, $N = 56$, Fig. 10a), most of which are monazite grains surrounded

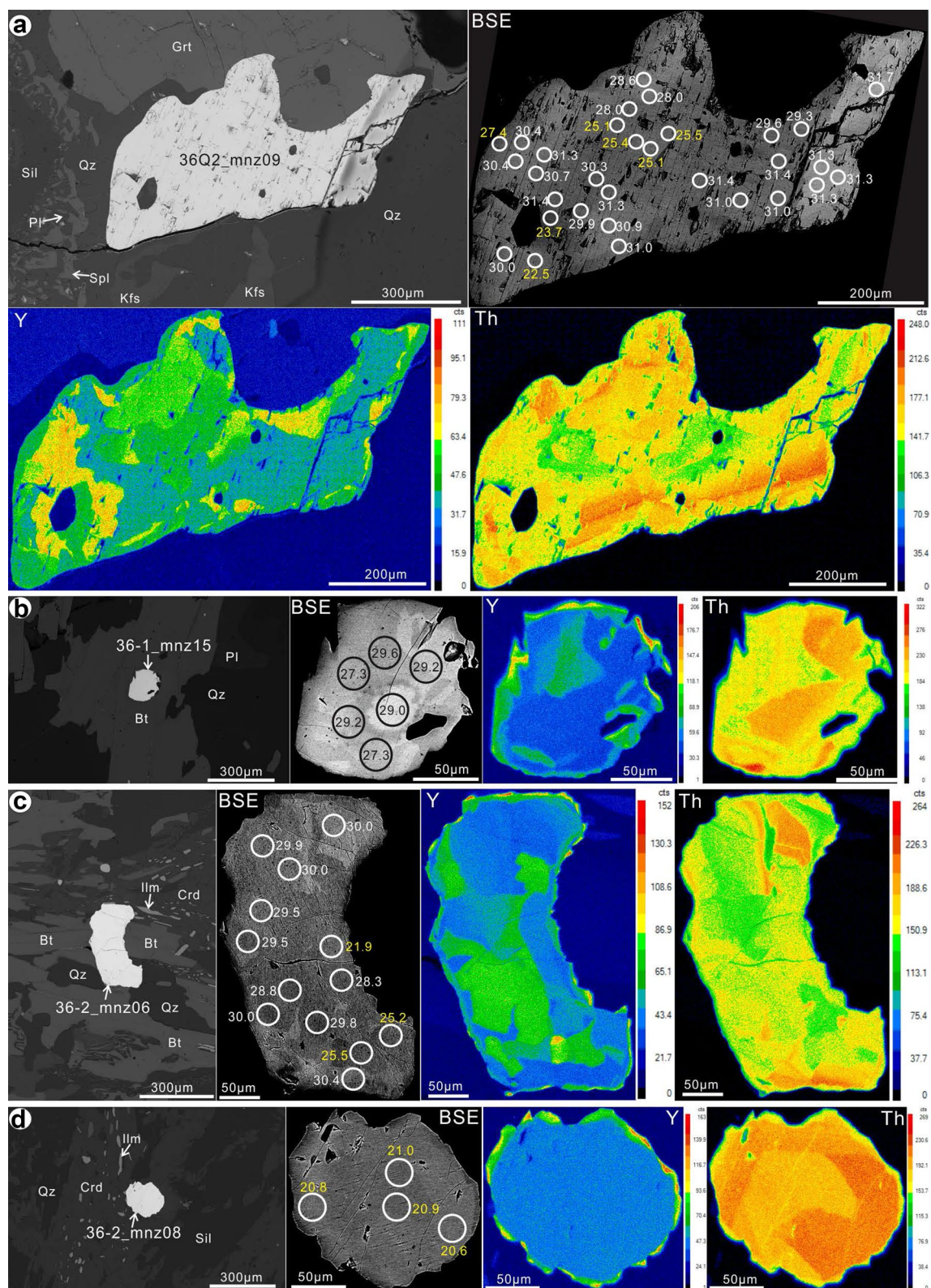


Fig. 9 Textural positions and Y and Th compositional mapping of representative monazite grains in sample 15DG36. Circles in the BSE images indicate the location of the laser pit and are ~24 μm in diameter, and the numbers indicate $^{208}\text{Pb}/^{232}\text{Th}$ ages in Ma. Warmer colours indicate higher concentrations of Y and Th

ter, and the numbers indicate $^{208}\text{Pb}/^{232}\text{Th}$ ages in Ma. Warmer colours indicate higher concentrations of Y and Th

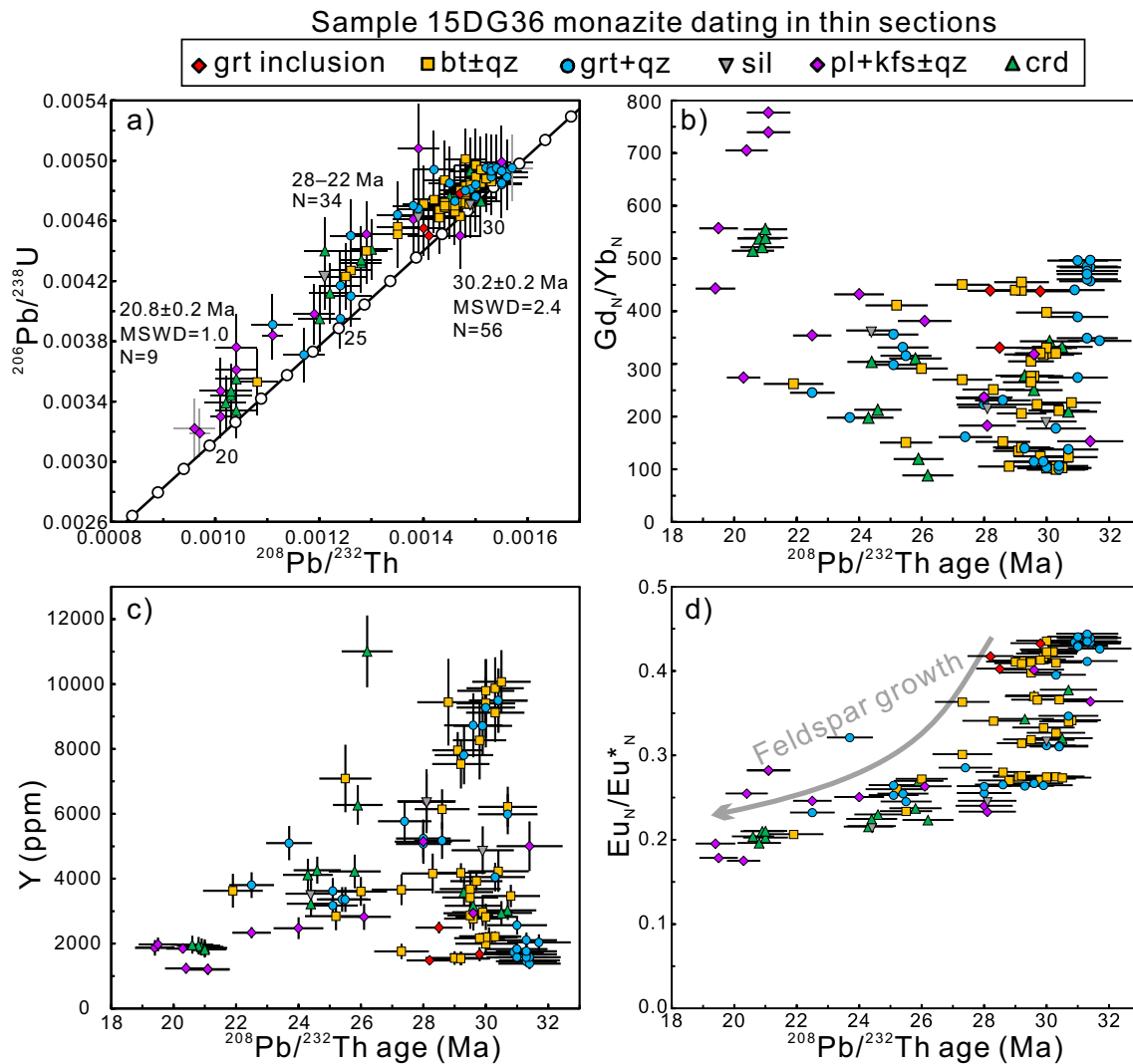


Fig. 10 Dating results for monazite in thin sections from sample 15DG36 highlighting the textural positions of monazite grains with co-existing minerals. **a** $^{208}\text{Pb}/^{232}\text{Th}$ versus $^{206}\text{Pb}/^{238}\text{U}$ concor-

dia plot of age data. **b** $^{208}\text{Pb}/^{232}\text{Th}$ age versus $\text{Gd}_\text{N}/\text{Yb}_\text{N}$ ratio plot. **c** $^{208}\text{Pb}/^{232}\text{Th}$ age versus Y concentration plot. **d** $^{208}\text{Pb}/^{232}\text{Th}$ age versus Eu anomaly plot

by biotite ± quartz and garnet + quartz, and those that are included in garnet. A younger cluster of ages is at 20.8 ± 0.2 Ma (MSWD 1.0, $N = 9$), all of which are from monazite grains surrounded by cordierite or plagioclase + K-feldspar ± quartz (likely leucosome). A few grains yield intermediate ages of 28–22 Ma ($N = 34$) that are more scattered. The relationship between ages and REE or Y compositions is weak. Monazite grains that yield dates 30–23 Ma have variable Y and HREE contents (Y 1500–11,500 ppm, $\text{Gd}_\text{N}/\text{Yb}_\text{N}$ 100–500). Domains that yield younger dates have relatively low Y and HREE contents (Y 1200–3600 ppm, $\text{Gd}_\text{N}/\text{Yb}_\text{N}$ 300–800, Fig. 10b, c). Negative Eu anomaly gradually increases from older dates to younger ones (0.45–0.18, Fig. 10d).

Zircon U–Pb dating

Zircon grains from migmatitic metapelites 15DG36 and 15DG40 are generally rounded (Fig. 11) and present a complex core–mantle–rim structure. The cores are small in size (most <30 μm) with CL-bright oscillatory zoning, and the mantles are CL-dark; the rims are CL-bright and some rims have weak oscillatory zoning (Fig. 11a). A few grains appear unzoned or have weak sector zoning and are equivalent to the rims in CL-emission (Fig. 11b). In sample 15DG36, the cores yield inherited $^{207}\text{Pb}/^{206}\text{Pb}$ dates of 900–818 Ma ($N = 6$) with one older analysis at 2524 ± 19 Ma (Online Resource Fig. S3e). Zircon mantles define an age of 29.7 ± 0.6 Ma (MSWD 2.6, $N = 12/15$), whereas rims ages

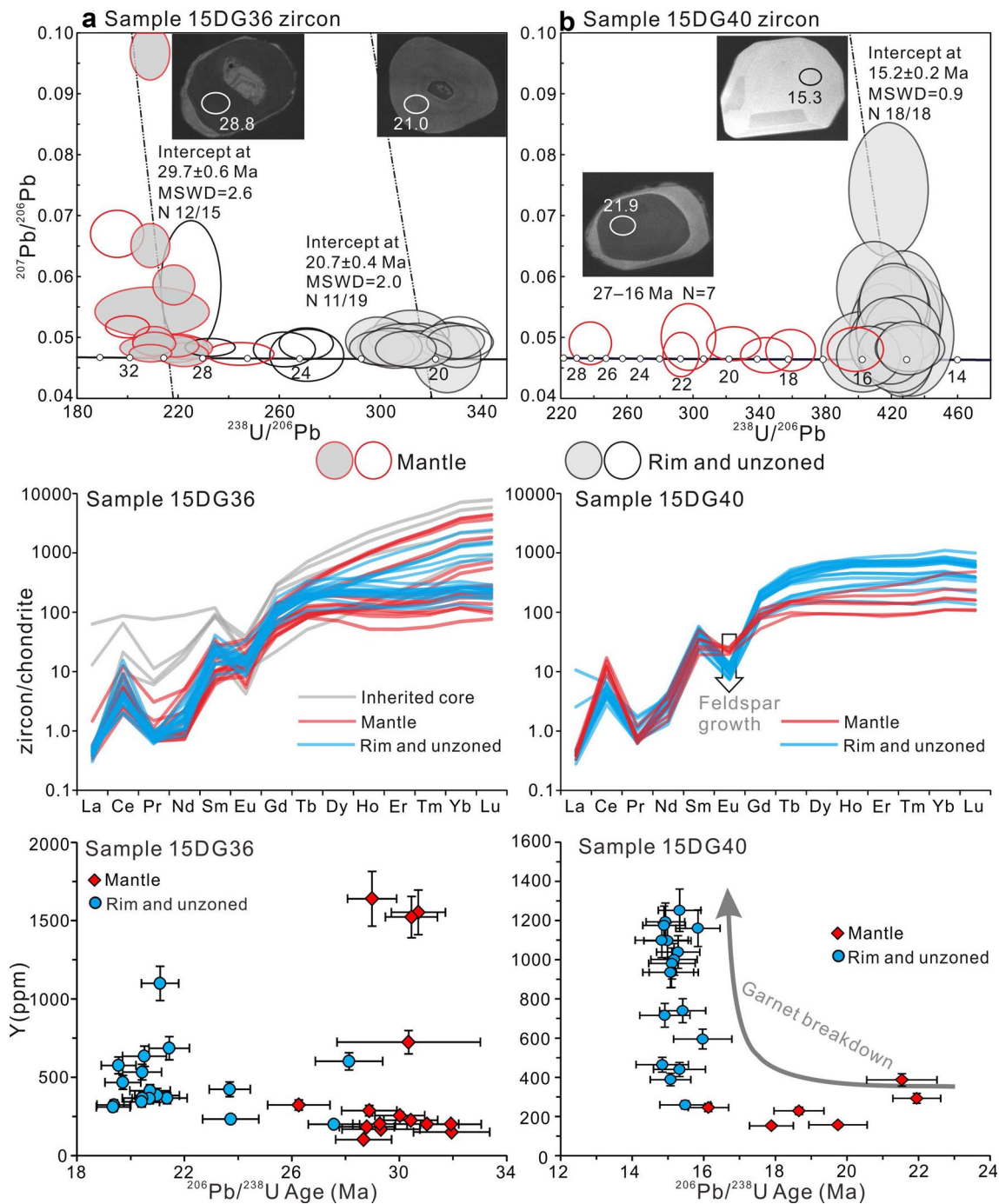


Fig. 11 Zircon geochronology and trace element results from samples 15DG36 (**a**) and 15DG40 (**b**). Ellipses in the cathode-luminescence images indicate the location of the ion beam pit and are ~25 μm in diameter, and the numbers indicate $^{206}\text{Pb}/^{238}\text{U}$ ages in

Ma. Errors are quoted at 2σ level. Only filled ellipses were used for intercept age calculation. The arrows highlight changes in heavy rare earth elements and Eu between different growth zones. Normalizing values are from McDonough and Sun (1995)

scatter and most rims yield an age of 20.7 ± 0.4 Ma (MSWD 2.0, N 11/19). Th/U ratios are higher in the inherited cores (0.14–0.95) and lower in the mantle and rim domains (0.01–0.07, Online Resource Fig. S4). Y and HREE contents show large variations, but the majority of mantle and

rims analyses have a flat HREE pattern (Fig. 11a); negative Eu anomaly generally overlaps between domains (Online Resource Table S6). Cores in sample 15DG40 are too small to be dated, mantles yield dates scattering between 27 and 16 Ma ($N = 7$, Th/U = 0.05–0.15), and rims are consistent

at 15.2 ± 0.2 Ma (MSWD 0.9, N 18/18, Th/U = 0.09–0.67). Rims are richer in Y, and show a stronger negative Eu anomaly than the mantles (Fig. 11b). Both mantle and rim have a flat HREE pattern. Mineral inclusions are plagioclase, biotite and quartz and no minerals indicative of specific metamorphic grades were observed.

Discussion

P–T evolution of the studied samples

Monazite growth in metasedimentary rocks has been related to metamorphic reactions and temperature (Catlos et al. 2002; Wing et al. 2003; Rubatto et al. 2013; Dumond et al. 2015) and thus age interpretation requires knowledge of the P–T paths of the studied samples. Mineral assemblages observed in this study suggest that the metapelitic samples from the GHC of Dinggye region recorded three stages of metamorphism: (a) an early stage at relatively high-pressure (M_1) represented by relict kyanite and rutile; (b) a phase at high-temperature and medium-pressure (M_2) represented by the dominant mineral assemblage $\text{Grt} \pm \text{Sil} + \text{Pl} + \text{Bt} + \text{Kfs} + \text{Qz} + \text{Rt} \pm \text{Ilm}$; (c) and overprint during isothermal decompression (M_3) represented by cordierite corona or spinel-plagioclase symplectite. Within this evolution, samples collected from the same tectonic unit may have equilibrated at different pressure conditions (e.g., Borghi et al. 2003). The investigated samples were collected from similar structural levels or close positions, and are not separated by tectonic discontinuities (see discussion below).

The calculated P–T results plot in the granulite-facies field with variable equilibrium pressures (Fig. 5, 5–10 kbar and 740–830 °C). These conditions correspond to the M_2 or M_3 stage instead of the presumed pressure peak for which there are only limited mineral relicts. Results from garnet-biotite thermometry (740–790 °C) could be lower than true peak temperatures due to possible disturbance from retrograde Fe–Mg exchange reactions or volume diffusion (Florence and Spear 1995). Temperature results from the Zr-in-rutile thermometer (760–820 °C) are slightly higher and are preferred as this thermometer is retentive at temperatures in excess of 900 °C (Jiao and Guo 2011; Kooijman et al. 2012; Ewing et al. 2013). For slowly cooled terranes, it may be possible for zirconium in rutile to undergo diffusional loss (e.g., Kelsey and Hand 2015), but for fast-cooled terranes like the Himalayas, zirconium diffusion in rutile is insignificant at these temperatures. In addition, we tried to avoid zirconium diffusion by locating the analyses away from the rims and excluding those that yield lower Zr values. The Zr-in-rutile estimates are the recorded highest metamorphic temperatures (early M_2) before rutile reacts to form ilmenite at low-pressure conditions (late M_2 or M_3). One P–T

estimate by GB-GASP thermobarometer (sample 15DG37) plots outside the sillimanite stability field probably because the temperature is underestimated. Nevertheless, the estimate by Zr-in-rutile thermometer and GASP barometer of sample 15DG37 is consistent with its equilibrium mineral assemblage. By combining the P–T estimates with observed assemblages, an isothermal decompression P–T path is reconstructed. Because the pressure estimates are based on assemblages equilibrated at the M_2 or M_3 stage, the pressure condition of the M_1 -stage should be higher (>10 kbar) based on the presence of kyanite relicts, but the temperatures are probably indistinguishable. Generally, the estimated pressures seem to decrease slightly from south (10–7 kbar) to north (6–5 kbar). However, it would be misleading to indicate maximum burial depths and identify metamorphic discontinuities using these pressure conditions because in some samples the thermobarometry may have been compromised by diffusional re-equilibration and only return minimum values.

When the P–T conditions calculated for all samples are plotted into the phase diagram constructed using the specific bulk composition of sample 15DG36 (Fig. 5a and Online Resource Fig. S1), they match well the observed assemblages and it may be inferred that: (i) the first melt in the Dinggye pelitic granulites was possibly produced by muscovite dehydration-melting reaction (R1) during the prograde stage; afterwards, back-reaction of R1 crystallized muscovite as part of the polymineralic inclusions in garnet; (ii) biotite dehydration-melting by reaction (R2) occurred during the early M_2 -stage; (iii) during the final decompression stage, the P–T path entered the cordierite stability field by consuming garnet (R3 and R4). The shape of the reconstructed P–T path is consistent with previous results for the GHC pelitic granulites in this area (Fig. 5b, Borghi et al. 2003). However, P–T estimates from Borghi et al. (2003) are within the amphibolite-facies field because that study only used major element thermometry and may have underestimated the temperatures. The morphology and conditions of the reconstructed P–T path resemble those of the cordierite-spinel bearing high-pressure pelitic granulites from a similar structural level of the GHC in Sikkim (from 12–9 kbar to 5–3 kbar, 750–800 °C, Sorcar et al. 2014).

Linking monazite and zircon ages to metamorphic stages

A rigorous interpretation of monazite and zircon ages requires for the growth of accessory minerals that yield different Himalayan ages to be linked to specific metamorphic stages. This is particularly important and challenging for monazite ages interpretation because this mineral can form at various stages along a metamorphic P–T cycle (see a summary in the introduction). In this study, some general

criteria are used. (a) Date of a monazite domain with a mineral inclusion should record a metamorphic stage later than or coeval with the growth of the trapped mineral. (b) The age of monazite included in a host phase constrains the time of growth of the host phase if the monazite was in equilibrium at entrapment (e.g., Catlos et al. 2002; Foster et al. 2002; Kohn et al. 2004; From et al. 2014; Carosi et al. 2016), or the monazite age predates the host phase age if it did not equilibrate at time of entrapment (Kohn 2016). (c) Monazite chemical zonation may indicate growth mechanisms if combined with other criteria. Monazite HREE and Y signatures are controlled by garnet in a xenotime-absent closed system: garnet growth reduces HREE and Y in monazite, and garnet breakdown redistributes HREE and Y into monazite (Schaltegger et al. 1999; Foster et al. 2002; Kohn and Malloy 2004; Rubatto et al. 2006). Negative Eu anomaly in monazite may reflect increasing feldspar proportions, such as K-feldspar growth through muscovite or biotite dehydration-melting reactions (Rubatto et al. 2013; Wang et al. 2015a). However, monazite behaviour in granulite-facies metamorphism can be further complicated by open system (Harley and Nandakumar 2014) and possible melt loss (Yakymchuk and Brown 2014), and chemical correlations have been shown to fail in a few cases (Hokada and Motoyoshi 2006; Kelly et al. 2012). Therefore, the interpretation below relies on multiple constraints. Similar criteria apply to zircon. Monazite and zircon dates in this study could be classified into four groups.

Inherited dates

Monazites cores in four samples yield inherited dates of 500–400 Ma (Fig. 12). A few patchy zoned cores or rims yield intermediate dates of 400–40 Ma that are scattering and either represent physical core-rim mixtures or core ages that have undergone Pb loss during Himalayan metamorphism. Despite a high volume diffusion closure temperature for Pb in monazite under dry conditions (Cherniak et al. 2004), Pb loss or partial resetting of ages through monazite recrystallization or dissolution–precipitation is possible even at low-temperature conditions (<600 °C) if the system is buffered with melt or fluid (Seydoux-Guillaume et al. 2002; Williams et al. 2011; Grand'Homme et al. 2016). The 500–400 Ma dates are taken as inherited ages and agree with previous data from Himalayan (meta)sediments (e.g., DeCelles et al. 2000; Martin et al. 2007) or GHC granitic orthogneiss (e.g., Cawood et al. 2007). However, evidences from this study are not sufficient to make further interpretation whether these inherited monazite dates represent an early Palaeozoic regional metamorphism or a thermal event related to the intrusion of large early Palaeozoic granites. Inherited zircon dates are older and scatter over a wider range, suggesting that the inherited zircon cores are detrital.

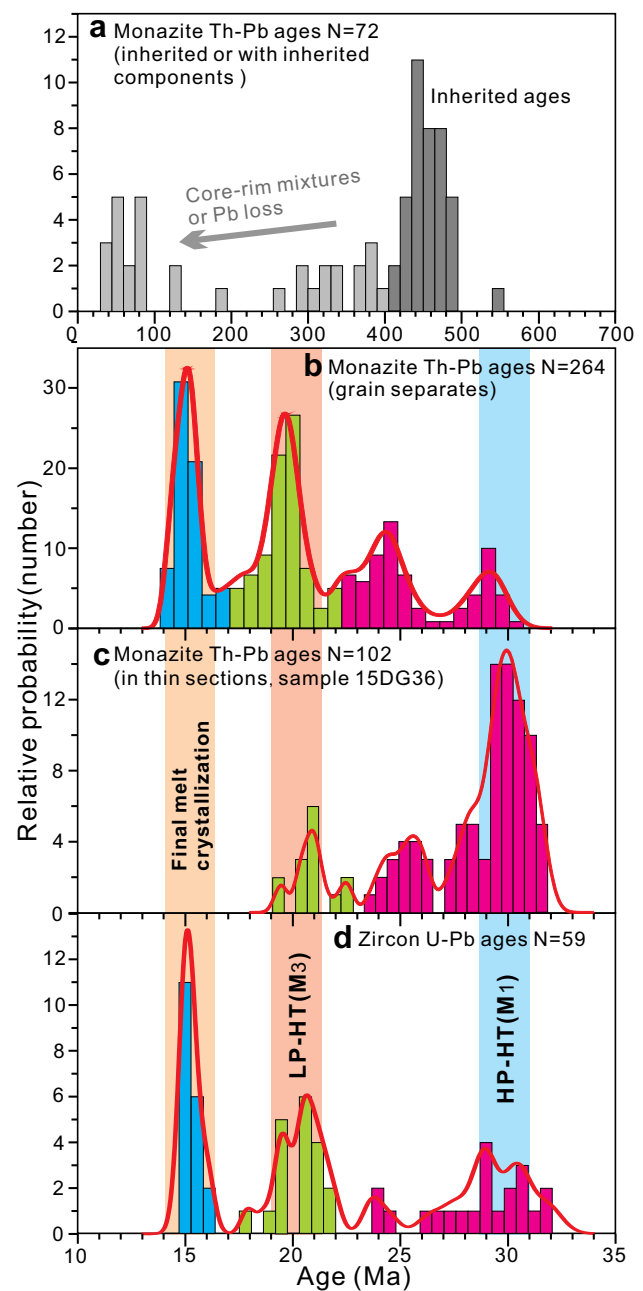


Fig. 12 Relative probability diagrams for monazite (a, b, c) and zircon (d) ages obtained from the investigated samples

Prograde melting at 30–29 Ma

The oldest metamorphic ages in pelitic granulites of this study are around ~30–29 Ma and are only preserved in sample 15DG36 from monazite and zircon (Fig. 12). Decreasing Y from the high Y cores toward the rims in some monazite grains (Fig. 9b, c) suggest that the ~30–29 Ma monazite domains formed during prograde metamorphism when garnet proportion was increasing. It is unlikely that these domains formed at sub-solidus conditions because some

of the ~30 Ma domains contain polymineralic inclusions of K-feldspar + quartz \pm muscovite, which are interpreted as ‘nanogranites’ and represent crystallized melt (Cesare et al. 2009, 2015; Ferrero et al. 2012). Nanogranite inclusions in monazite were trapped when or after the P–T path reached supra-solidus conditions and crossed the K-feldspar-in curve at temperatures of >750–700 °C (Fig. 5a). Garnet grain could shield its monazite inclusions from Pb loss or growth of younger monazite (e.g., Foster et al. 2000; Catlos et al. 2002; Kohn 2016). Dated monazite inclusions in garnet, which are far away from fractures, yield ~30–29 Ma ages similar to the matrix monazites that coexist with biotite \pm quartz or garnet + quartz, suggesting that ~30–29 Ma ages constrain metamorphic conditions approaching the peak. We thus conclude that the ~30–29 Ma ages in both monazite and zircon from sample 15DG36 formed during prograde melting close to the M_1 stage.

Isothermal decompression at 25–19 Ma

The ~21–19 Ma dates are most abundant and are recorded in five samples either in monazite or zircon (Fig. 12). Abundant sillimanite and polymineralic ‘nanogranite’ inclusions of K-feldspar + quartz \pm muscovite \pm plagioclase are present in the ~21–19 Ma monazite domains and suggest that these domains are coeval or younger than the M_2 stage. Increase of Y from ~22 Ma to ~17 Ma in 15DG37 monazite (Online Resource Fig. S2b) and increase of HREE from ~25 Ma to ~24 Ma in 15DG66 monazite (Fig. 7b) suggest that these ages are coeval or younger than garnet breakdown (M_2 – M_3). Monazite hosted by cordierite (Fig. 9d) yields ~21–20 Ma ages in sample 15DG36, which gives the tightest constraint that the ~21–19 Ma dates represent the timing of the M_3 stage. Therefore, we suggest that the ~25–19 Ma ages represent a prolonged decompression and melting (M_2 – M_3) and ~21–19 Ma ages mark the end of this decompression (M_3).

Final melt crystallization at ~15 Ma

The ~15 Ma dates are recorded in three samples by monazite and one sample by zircon (Fig. 12). As described above, possible interpretations for young monazite ages are recrystallization during retrograde fluid alteration or growth during final melt crystallization. The second interpretation is more likely to account for our case because: (a) melt inclusions were observed in the ~15 Ma dates monazite; (b) hydrothermal monazite or monazite altered by retrograde fluid usually occurs along grain boundaries, internal fractures, or in clusters of multiple tiny grains (e.g., Schandl and Gorton 2004; Williams et al. 2007; Taylor et al. 2014), whereas most monazite grains with ~15 Ma dates are unzoned, homogeneous and relatively large in size (100–200 μ m); (c) hydrothermal monazite commonly has very low ThO₂ concentrations

(<1 wt%) and Eu anomalies are commonly small or absent (e.g., Zhu and O’Nions 1999; Smith et al. 2000; Schandl and Gorton 2004; Williams et al. 2007), whereas the ~15 Ma monazite grains have high ThO₂ content (5–8 wt%) and a medium to strong negative Eu anomaly; (d) alteration of zircon during retrogression is rare and generally along grain boundaries or fractures (Carson et al. 2002), whereas the ~15 Ma zircon grains in the investigated samples have sector zoning or are unzoned, which resembles those crystallized from an anatectic melt (e.g., Taylor et al. 2016). Therefore, we suggest that the ~15 Ma age constrain the final melt crystallization in the migmatites. Melt crystallization in the migmatites is coeval with leucogranite emplacement (~14 Ma, sample 15DG96, this study; 16–14 Ma, Cottle et al. 2009a; Leloup et al. 2010), suggesting cooling of the GHC below solidus in the Dinggye region.

Monazite and zircon geochronology constrains the time-scale of metamorphism of the GHC in the Dinggye Himalaya (Figs. 5, 12). The three groups of metamorphic ages cannot be related to hidden tectonic discontinuities because they can be obtained in samples from one location (e.g., samples 15DG35, 36, 37 and 40 from Kharta). Additionally, no tectonic discontinuities have ever been reported in the Dinggye region; the widely addressed High Himalayan Discontinuity or High Himal Thrust (Goscombe et al. 2006; Imayama et al. 2010, 2012) is located further south of our samples (Fig. 1). Notably, the ~20 Ma and ~15 Ma dates obtained in samples from the Kharta transect (this study) have also been found in the Thongmön transects (Cottle et al. 2009a) suggesting that the GHC in the Kharta-Thongmön transects underwent a coeval evolution.

Monazite behaviour during isothermal decompression

The investigation of monazite behaviour during isothermal decompression is aimed to establish: (a) what process/reaction triggered monazite growth during partial melting; (b) how inherited monazites or monazites that formed during the M_1 stage survived prolonged partial melting (>10 Myr) in the Dinggye Himalaya.

Solubility not high enough to dissolve all the inherited monazite

Inherited monazite has been widely documented in the Himalaya metamorphic rocks (e.g., Harrison et al. 1995; Martin et al. 2007; Rubatto et al. 2013; Warren et al. 2014; Wang et al. 2015a). In the Dinggye Himalaya, inherited monazites are more common than other Himalayan transects despite the fact that Dinggye samples underwent a similar or even higher-temperature granulite-facies metamorphism. This suggests that monazite solubility at granulite-facies temperatures

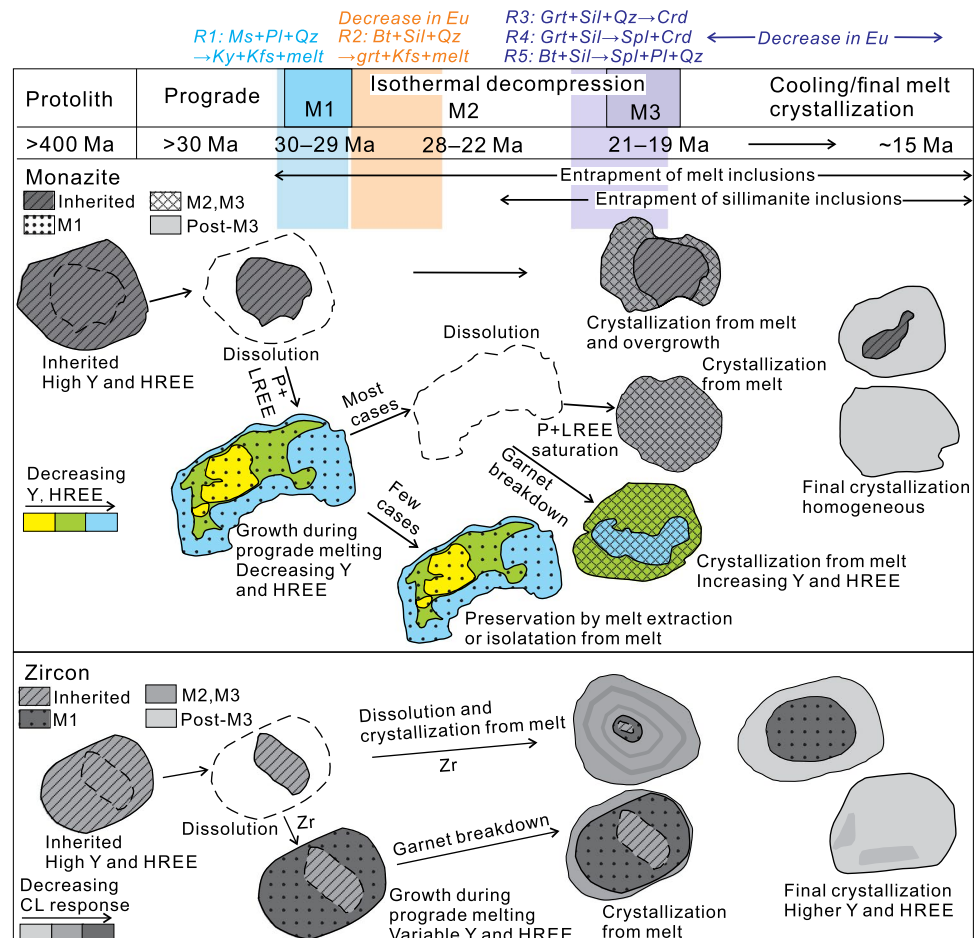
may be less than what previously reported and implemented in early phase equilibria modelling (see Kelsey et al. 2008), which simply used the equations of Rapp and Watson (1986). Some other studies suggest relatively lower solubility of monazite in peraluminous melt (Montel 1993; Stepanov et al. 2012) and recent models by Yakymchuk and Brown (2014) are more compatible with observations from this study, supporting potential preservation of inherited or prograde monazite in granulite-facies melt. Despite a relatively low solubility, other factors such as textural position and kinetics may also contribute to preservation of the inherited monazite but need to be evaluated case by case. It is noticed that the HREE contents of the inherited domains in both monazite and zircon are higher than that of the metamorphic domains (samples 15DG35, 47 and 36, Figs. 7, 11a, 13). This may be caused by absent of garnet in the protolith or pre-Himalayan metamorphic event versus garnet presence during Himalayan metamorphism, although the garnet proportion may have decreased during isothermal decompression.

Dissolution–precipitation at the M_1 stage

Evidences from this study show that monazites that preserved ~30–29 Ma ages formed during prograde melting approaching the M_1 stage. During prograde melting, muscovite dehydration-melting reaction (R1) can produce 5–10% percent of melt in water-saturated conditions (Groppo et al. 2012; Sorcar et al. 2014) and thus promoted dissolution of pre-existing sub-solidus or inherited monazite (Fig. 13). This provides the necessary phosphorus and LREE for monazite to grow, and new monazite that recorded ~30–29 Ma ages then precipitated from the M_1 -stage melt (Fig. 13). Such an interpretation is consistent with ‘nanogranite’ inclusions in monazite of sample 15DG36. Ages of monazite formed at this stage are undistinguishable throughout entire grains (Fig. 9a–c). During the prograde melting, many monazite grains present decreasing Y and HREE compositional zoning in equilibrium with garnet growth (Fig. 13), but some monazite grains have heterogeneous Y compositions that may be influenced by local reactive bulk Y contents (Fig. 9a).

During subsequent anatexis and biotite melting, monazite dissolution in the melt is an effective process. For the

Fig. 13 Schematic diagram showing monazite and zircon dissolution-crystallization processes in the metapelites of the Dinggye Himalaya during granulite-facies metamorphism. Monazite chemical composition signatures, related melting reactions and entrapment of index mineral inclusions are described as text in the diagram. Domains that have different ages or compositions are differentiated by different designs (see the left portion for explanation). The dashed line marks the dissolution limit for the monazite or zircon grains at each certain stage



M_1 -stage monazite in sample 15DG36, the subsequent prolonged isothermal decompression process (see discussion below) will enhance the chance for these grains to be dissolved. Previous studies highlighted the shield effect of garnet to preserve prograde or peak metamorphic ages in monazite (Foster et al. 2000; Catlos et al. 2002; Martin et al. 2007), whereas biotite and quartz are not usually regarded as good containers. In this study, the ~30–29 Ma monazite grains that yield prograde ages are more commonly in contact with matrix minerals such as biotite and quartz (Fig. 9b, c). One possible interpretation is that some matrix minerals, to a lesser extent, could isolate the monazite from melt and protect it from dissolving (Fig. 13), an interpretation that was also suggested by Simpson et al. (2000) based on preserved Oligocene monazites from the nearby Everest region. A more likely interpretation is that rapid melt mobilization and extraction could isolate monazite from melt (Fig. 13) and prevent dissolution (see discussion in Yakymchuk and Brown 2014). Whenever monazite is in contact with cordierite or leucosome, more commonly it yields younger ages (Fig. 10a).

Dissolution and crystallization at the M_2 – M_3 stage

At the early stages of decompression (early M_2 stage), the samples gradually reached the temperature peak and partial melting volumes of 20–25%, which were mainly produced by biotite dehydration-melting reaction R2. With such high degrees of partial melting, monazites were mainly being dissolved (Fig. 13). During the late stage of M_2 , few monazite grains precipitated earlier from the melt (sample 15DG66). At the end of the isothermal decompression (M_3 stage, ~21–19 Ma), monazite saturation was reached in many leucosomes, and abundant monazite crystallized from the melt and formed either new grains or overgrowth rims around pre-existing grains (Fig. 13), which is recorded by samples 15DG36, 37, 35, 47 and 50. An important feature for some monazites at this stage is increasing HREE or Y (Fig. 13), suggesting that the melt they crystallized from incorporated those HREE and Y released by garnet breakdown reaction R3 or R4 (e.g., Foster et al. 2002; Rubatto et al. 2013). Because K-feldspar crystallized during melt crystallization, these monazites also recorded a stronger negative Eu anomaly (Fig. 13).

Growth during final melt crystallization

During final melt crystallization (retrograde cooling, ~15 Ma), monazite and zircon will precipitate from the melt accommodating most of the remaining phosphorus + LREE and Zr, respectively, and forming unzoned new grains or overgrowth rims around pre-existing grains (Fig. 13). Compositions of these monazites and zircons are relatively

homogeneous among different grains. Their HREE and Y signatures depend on the chemical compositions of the crystallizing melt. However, it could be difficult to distinguish monazites that crystallized at final melt crystallization from those formed during isothermal decompression only based on zoning and compositions, and textural information must be combined.

In general, dating an individual sample may fail to extract time information of the three different metamorphic stages described above, because one sample may only record one of the stages due to variable influences such as melt loss (Harley and Nandakumar 2014; Yakymchuk and Brown 2014), complete or partial resetting of U–Th–Pb system (e.g., Seydoux-Guillaume et al. 2002; Williams et al. 2011), or dissolution of previous monazite (Kelsey et al. 2008; Bhowmik et al. 2014). Therefore, multiple samples are required to precisely constrain the different metamorphic stages along a P–T trajectory as indicated from the Dinggye Himalaya.

Pressure–temperature–time evolution of the Dinggye Himalaya

In the Dinggye Himalaya, we reconstructed an isothermal decompression P–T path from the GHC pelitic granulites (>10 kbar to ~5 kbar, ~750–830 °C, Fig. 5). Such a P–T path resembles the isothermal decompression path from the ADM granulitized eclogite (Groppo et al. 2007; Wang et al. 2017), but the recorded peak pressure condition from the GHC pelitic granulites is lower. An eclogite-facies metamorphism of the ADM granulitized eclogite has been widely supposed, which was firstly based on clinopyroxene-plagioclase symplectite (suggesting breakdown from omphacite, Groppo et al. 2007) and then omphacite inclusions in garnet (Jd ~28–22%, Wang et al. 2017). In fact, clinopyroxene-plagioclase symplectites are widespread within the GHC high-pressure mafic granulite from Thongmön (Li et al. 2003; Liu et al. 2007; Cottle et al. 2009a) or the Arun river valley (Corrie et al. 2010), and omphacite inclusion is also present in the GHC mafic granulite in Thongmön (Jd ~28%, our unpublished data). However, it remains unclear whether the mafic HP granulite/eclogite and its country rocks (pelitic granulites) within the GHC were buried/subducted to 60–70 km depth as supposed by previous studies (Fig. 5b) because omphacite could form at pressure of ~15 kbar at temperature of >600 °C (Groppo et al. 2007). It is however clear that the GHC mafic and pelitic granulites underwent the M_1 -stage high-pressure metamorphism and subsequent exhumation together.

Our results suggest that the high-pressure granulite-facies metamorphism (M_1) within the GHC of Dinggye occurred at ~30–29 Ma. This is overall consistent with the peak Barrovian/high-pressure metamorphism of the upper GHC in the central portion of the Himalaya (e.g., Simpson et al. 2000;

Searle et al. 2003; Cottle et al. 2009a; Carosi et al. 2010; Groppo et al. 2010; Imayama et al. 2012; Rubatto et al. 2013; Wang et al. 2015a; Zhang et al. 2017), suggesting that the upper portion of the GHC was exhumed together. Despite high-pressure metamorphism at ~30–29 Ma, zircons in the GHC mafic granulites only recorded U–Pb ages after the M_3 stage (~18–16 Ma, Li et al. 2003; Cottle et al. 2009a). This implies that an eclogite-facies metamorphism of the ADM at 38–34 Ma (Lu–Hf dating, Kellett et al. 2014) is more likely, whereas zircon U–Pb ages of the ADM granulitized eclogites (~14–13 Ma, Lombardo et al. 2016; Wang et al. 2017) perhaps represent the timing of exhumation. Such an interpretation is more consistent with published monazite Th–Pb ages (13–12 Ma, Cottle et al. 2009b; Kali et al. 2010) from the ADM orthogneiss. The alternative scenario requires an exhumation rate of the ADM of one order of magnitude larger than that of the GHC (~1–2 mm/y), which is not supported by thermochronologic results (Jessup et al. 2008). For high-pressure rocks that were overprinted by high-temperature granulite-facies metamorphism, extracting the peak metamorphic timing is challenging. The timing of high-pressure metamorphism (~30–29 Ma) constrained from this study is of crucial importance to the continental thickening processes of the central Himalaya.

The timescale of metamorphism shows that low-pressure high-temperature metamorphism (M_3) occurred at ~21–19 Ma and melt crystallization (<650 °C) occurred at ~15 Ma. This implies that isothermal decompression (M_2 – M_3) was sustained for ~10 Myr and cooling from ~750–800 °C to <650 °C took ~5 Myr. The calculated cooling rate for the upper GHC matches the published results for the initial retrograde stage (40–30 °C/Myr, Kohn 2008; Imayama et al. 2012; Wang et al. 2015a). The geothermal gradient during the M_3 stage would be as high as ~45 °C/km, much higher than a stable crustal geotherm (~25 °C/km). The high geothermal gradient and relatively long duration of isothermal decompression (~10 Myr) suggest that exhumation of the GHC was assisted by partial melting. This supports previous numerical simulation studies that melt could lower the viscosity of the continental crust and trigger exhumation of high-grade metamorphic rocks during continent–continent collision (Beaumont et al. 2001; Jamieson et al. 2004; Faccenda et al. 2008).

Conclusion

Pelitic granulites from the GHC of Dinggye Himalaya underwent a P–T evolution marked by isothermal decompression from kyanite-grade high-pressure metamorphism (M_1), to sillimanite-grade metamorphism (M_2) or cordierite-grade metamorphism (M_3) with equilibrium P–T conditions of 5–10 kbar and 750–830 °C. Monazite and zircon in nine

pelitic and psammitic granulites record either inherited ages or metamorphic ages at various stages within this metamorphic cycle. Inherited monazite domains (500–400 Ma) are widely preserved even at granulite-facies conditions. Few monazite and zircon grains recorded ages close to the M_1 -stage (~30–29 Ma), and formed during prograde metamorphism, likely by muscovite dehydration-melting. These monazite grains were either protected by matrix minerals from later dissolution in the melt, or escaped dissolution because of melt extraction. During initial decompression, most of the inherited or prograde monazite grains were dissolved into the melt mainly produced by biotite dehydration-melting. Abundant monazite grains crystallized from melt at the end of decompression (M_3 -stage, 21–19 Ma) and are chemically related to garnet breakdown reactions. During final melt crystallization (~15 Ma), a few more monazite grains with homogeneous compositions crystallized from the melt. The constructed P–T–time path indirectly constrains the timing of peak high-pressure metamorphism (~30–29 Ma) in the central Himalaya even in the highly overprinted pelitic granulites. Isothermal decompression in Dinggye region was sustained for ~10 Myr during ~30–20 Ma, and is in line with a melt-assisted exhumation of the GHC rocks.

Acknowledgements The authors thank X.-H. Li, X.-X. Ling, Y.-H. Yang and Q. Mao for analytical help with the SIMS, LA-ICP-MS and EPMA. S. Chakraborty and S. Dasgupta are thanked for discussion. We appreciate two anonymous reviewers and editor F. Poitrasson for constructive comments. This work was supported by the National Natural Science Foundation of China (Grant Numbers 41602054, 41402055 and 41130313), China Postdoctoral Science Foundation (Grant Numbers 2015LH0002 and 2016M600126) and China Geological Survey (Grant Number 201306010046).

References

- Akers WT, Grove M, Harrison TM, Ryerson FJ (1993) The instability of rhabdophane and its unimportance in monazite paragenesis. *Chem Geol* 110(1):169–176. doi:[10.1016/0009-2541\(93\)90252-E](https://doi.org/10.1016/0009-2541(93)90252-E)
- Aleinikoff JN, Schenck WS, Plank MO, Srogi L, Fanning CM, Kamo SL, Bosbyshell H (2006) Deciphering igneous and metamorphic events in high-grade rocks of the Wilmington Complex, Delaware: morphology, cathodoluminescence and backscattered electron zoning, and SHRIMP U–Pb geochronology of zircon and monazite. *Geol Soc Am Bull* 118(1–2):39–64. doi:[10.1130/b25659.1](https://doi.org/10.1130/b25659.1)
- Arita K (1983) Origin of the inverted metamorphism of the lower Himalayas, Central Nepal. *Tectonophysics* 95(1–2):43–60. doi:[10.1016/0040-1951\(83\)90258-5](https://doi.org/10.1016/0040-1951(83)90258-5)
- Beaumont C, Jamieson RA, Nguyen M, Lee B (2001) Himalayan tectonics explained by extrusion of a low-viscosity crustal channel coupled to focused surface denudation. *Nature* 414:738–742. doi:[10.1038/414738a](https://doi.org/10.1038/414738a)
- Bhowmik SK, Wilde SA, Bhandari A, Basu Sarbadhikari A (2014) Zoned monazite and zircon as monitors for the thermal history of

- granulite terranes: an example from the Central Indian Tectonic Zone. *J Petrol* 55:585–621. doi:[10.1093/petrology/egt078](https://doi.org/10.1093/petrology/egt078)
- Borghesi A, Castelli D, Lombardo B, Visonà D (2003) Thermal and baric evolution of garnet granulites from the Kharta region of S Tibet, E Himalaya. *Eur J Miner* 15(2):401–418. doi:[10.1127/0935-1221/2003/0015-0401](https://doi.org/10.1127/0935-1221/2003/0015-0401)
- Burchfiel B, Royden LH (1985) North-south extension within the convergent Himalayan region. *Geology* 13(10):679–682. doi:[10.1130/0091-7613\(1985\)13<679:newtch>2.0.co;2](https://doi.org/10.1130/0091-7613(1985)13<679:newtch>2.0.co;2)
- Burchfiel BC, Zhiliang C, Hodges KV, Yuping L, Royden LH, Changrong D, Jiene X (1992) The South Tibetan Detachment System, Himalayan Orogen: extension contemporaneous with and parallel to shortening in a Collisional Mountain Belt. *Geol Soc Am Spec Pap* 269:1–41. doi:[10.1130/SPE269-p1](https://doi.org/10.1130/SPE269-p1)
- Carosi R, Montomoli C, Rubatto D, Visonà D (2010) Late Oligocene high-temperature shear zones in the core of the Higher Himalayan Crystallines (Lower Dolpo, western Nepal). *Tectonics* 29:TC4029. doi:[10.1029/2008tc002400](https://doi.org/10.1029/2008tc002400)
- Carosi R, Montomoli C, Rubatto D, Visonà D (2013) Leucogranite intruding the South Tibetan Detachment in western Nepal: implications for exhumation models in the Himalayas. *Terra Nova* 25(6):478–489. doi:[10.1111/ter.12062](https://doi.org/10.1111/ter.12062)
- Carosi R, Montomoli C, Iaccarino S, Massonne H-J, Rubatto D, Langone A, Gemignani L, Visonà D (2016) Middle to late Eocene exhumation of the Greater Himalayan Sequence in the Central Himalayas: progressive accretion from the Indian plate. *Geol Soc Am Bull* 128(11–12):1571–1592. doi:[10.1130/b31471.1](https://doi.org/10.1130/b31471.1)
- Carson CJ, Ague JJ, Grove M, Coath CD, Harrison TM (2002) U–Pb isotopic behaviour of zircon during upper-amphibolite facies fluid infiltration in the Napier Complex, east Antarctica. *Earth Planet Sci Lett* 199(3–4):287–310. doi:[10.1016/S0012-821X\(02\)00565-4](https://doi.org/10.1016/S0012-821X(02)00565-4)
- Catlos EJ, Gilley LD, Harrison TM (2002) Interpretation of monazite ages obtained via in situ analysis. *Chem Geol* 188(3–4):193–215. doi:[10.1016/S0009-2541\(02\)00099-2](https://doi.org/10.1016/S0009-2541(02)00099-2)
- Cawood PA, Johnson MRW, Nemchin AA (2007) Early Palaeozoic orogenesis along the Indian margin of Gondwana: tectonic response to Gondwana assembly. *Earth Planet Sci Lett* 255(1–2):70–84. doi:[10.1016/j.epsl.2006.12.006](https://doi.org/10.1016/j.epsl.2006.12.006)
- Cesare B, Ferrero S, Salvioli-Mariani E, Pedron D, Cavallo A (2009) “Nanogranite” and glassy inclusions: the anatectic melt in migmatites and granulites. *Geology* 37(7):627–630. doi:[10.1130/g25759a.1](https://doi.org/10.1130/g25759a.1)
- Cesare B, Acosta-Vigil A, Bartoli O, Ferrero S (2015) What can we learn from melt inclusions in migmatites and granulites? *Lithos* 239:186–216. doi:[10.1016/j.lithos.2015.09.028](https://doi.org/10.1016/j.lithos.2015.09.028)
- Chakraborty S, Anczkiewicz R, Gaidies F, Rubatto D, Sorcar N, Faak K, Mukhopadhyay D, Dasgupta S (2016) A review of thermal history and timescales of tectonometamorphic processes in Sikkim Himalaya (NE India) and implications for rates of metamorphic processes. *J Metamorph Geol* 34:785–803. doi:[10.1111/jmg.12200](https://doi.org/10.1111/jmg.12200)
- Cherniak DJ, Watson EB, Grove M, Harrison TM (2004) Pb diffusion in monazite: a combined RBS/SIMS study. *Geochim Cosmochim Acta* 68(4):829–840. doi:[10.1016/j.gca.2003.07.012](https://doi.org/10.1016/j.gca.2003.07.012)
- Clarke GL, Powell R (1991) Decompressional coronas and symplectites in granulites of the Musgrave Complex, central Australia. *J Metamorph Geol* 9(4):441–450. doi:[10.1111/j.1525-1314.1991.tb00538.x](https://doi.org/10.1111/j.1525-1314.1991.tb00538.x)
- Corrie SL, Kohn MJ (2011) Metamorphic history of the central Himalaya, Annapurna region, Nepal, and implications for tectonic models. *Geol Soc Am Bull* 123(9–10):1863–1879. doi:[10.1130/b30376.1](https://doi.org/10.1130/b30376.1)
- Corrie SL, Kohn MJ, Vervoort JD (2010) Young eclogite from the Greater Himalayan Sequence, Arun Valley, eastern Nepal: P–T–t path and tectonic implications. *Earth Planet Sci Lett* 289(3–4):406–416. doi:[10.1016/j.epsl.2009.11.029](https://doi.org/10.1016/j.epsl.2009.11.029)
- Cottle JM, Jessup MJ, Newell DL, Searle MP, Law RD, Horstwood MSA (2007) Structural insights into the early stages of exhumation along an orogen-scale detachment: the South Tibetan detachment system, Dzakaa Chu section, Eastern Himalaya. *J Struct Geol* 29(11):1781–1797. doi:[10.1016/j.jsg.2007.08.007](https://doi.org/10.1016/j.jsg.2007.08.007)
- Cottle JM, Searle Michael P, Horstwood Matthew SA, Waters David J (2009a) Timing of midcrustal metamorphism, melting, and deformation in the Mount Everest Region of Southern Tibet revealed by U–(Th)–Pb geochronology. *J Geol* 117(6):643–664. doi:[10.1086/605994](https://doi.org/10.1086/605994)
- Cottle JM, Jessup MJ, Newell DL, Horstwood MSA, Noble SR, Parrish RR, Waters DJ, Searle MP (2009b) Geochronology of granulitized eclogite from the Ama Drime Massif: implications for the tectonic evolution of the South Tibetan Himalaya. *Tectonics* 28(1):TC1002. doi:[10.1029/2008TC002256](https://doi.org/10.1029/2008TC002256)
- Cottle JM, Larson KP, Kellett DA (2015) How does the mid-crust accommodate deformation in large, hot collisional orogens? A review of recent research in the Himalayan orogen. *J Struct Geol* 78:119–133. doi:[10.1016/j.jsg.2015.06.008](https://doi.org/10.1016/j.jsg.2015.06.008)
- DeCelles PG, Gehrels GE, Quade J, LaReau B, Spurlin M (2000) Tectonic Implications of U–Pb Zircon Ages of the Himalayan Orogenic Belt in Nepal. *Science* 288(5465):497–499. doi:[10.1126/science.288.5465.497](https://doi.org/10.1126/science.288.5465.497)
- Dumond G, Goncalves P, Williams ML, Jercinovic MJ (2015) Monazite as a monitor of melting, garnet growth and feldspar recrystallization in continental lower crust. *J Metamorph Geol* 33(7):735–762. doi:[10.1111/jmg.12150](https://doi.org/10.1111/jmg.12150)
- Erickson TM, Pearce MA, Taylor RJM, Timms NE, Clark C, Reddy SM, Buick IS (2015) Deformed monazite yields high-temperature tectonic ages. *Geology* 43(5):383–386. doi:[10.1130/g36533.1](https://doi.org/10.1130/g36533.1)
- Ewing TA, Hermann J, Rubatto D (2013) The robustness of the Zr-in-rutile and Ti-in-zircon thermometers during high-temperature metamorphism (Ivrea-Verbano Zone, northern Italy). *Contrib Miner Petrol* 165(4):757–779. doi:[10.1007/s00410-012-0834-5](https://doi.org/10.1007/s00410-012-0834-5)
- Faccenda M, Gerya TV, Chakraborty S (2008) Styles of postsubduction collisional orogeny: influence of convergence velocity, crustal rheology and radiogenic heat production. *Lithos* 103(1–2):257–287. doi:[10.1016/j.lithos.2007.09.009](https://doi.org/10.1016/j.lithos.2007.09.009)
- Ferrero S, Bartoli O, Cesare B, Salvioli-Mariani E, Acosta-Vigil A, Cavallo A, Groppo C, Battistini S (2012) Microstructures of melt inclusions in anatectic metasedimentary rocks. *J Metamorph Geol* 30(3):303–322. doi:[10.1111/j.1525-1314.2011.00968.x](https://doi.org/10.1111/j.1525-1314.2011.00968.x)
- Ferry JM, Watson EB (2007) New thermodynamic models and revised calibrations for the Ti-in-zircon and Zr-in-rutile thermometers. *Contrib Miner Petrol* 154(4):429–437. doi:[10.1007/s00410-007-0201-0](https://doi.org/10.1007/s00410-007-0201-0)
- Florence FP, Spear FS (1995) Intergranular diffusion kinetics of Fe and Mg during retrograde metamorphism of a pelitic gneiss from the Adirondack Mountains. *Earth Planet Sci Lett* 134(3):329–340. doi:[10.1016/0012-821X\(95\)00129-Z](https://doi.org/10.1016/0012-821X(95)00129-Z)
- Foster G, Kinny P, Vance D, Prince C, Harris N (2000) The significance of monazite U–Th–Pb age data in metamorphic assemblages; a combined study of monazite and garnet chronometry. *Earth Planet Sci Lett* 181(3):327–340. doi:[10.1016/S0012-821X\(00\)00212-0](https://doi.org/10.1016/S0012-821X(00)00212-0)
- Foster G, Gibson HD, Parrish R, Horstwood M, Fraser J, Tindle A (2002) Textural, chemical and isotopic insights into the nature and behaviour of metamorphic monazite. *Chem Geol* 191(1–3):183–207. doi:[10.1016/S0009-2541\(02\)00156-0](https://doi.org/10.1016/S0009-2541(02)00156-0)
- From R, Larson K, Cottle JM (2014) Metamorphism and geochronology of the exhumed Himalayan midcrust, Likhu Khola region, east-central Nepal: recognition of a tectonometamorphic discontinuity. *Lithosphere* 10(2):292–307. doi:[10.1130/l381.1](https://doi.org/10.1130/l381.1)

- Goscombe B, Gray D, Hand M (2006) Crustal architecture of the Himalayan metamorphic front in eastern Nepal. *Gondwana Res* 10(3–4):232–255. doi:[10.1016/j.gr.2006.05.003](https://doi.org/10.1016/j.gr.2006.05.003)
- Grand'Homme A, Janots E, Seydoux-Guillaume A-M, Guillaume D, Bosse V, Magnin V (2016) Partial resetting of the U–Th–Pb systems in experimentally altered monazite: nanoscale evidence of incomplete replacement. *Geology* 44(6):431–434. doi:[10.1130/g37770.1](https://doi.org/10.1130/g37770.1)
- Groppo C, Lombardo B, Rolfo F, Pertusati P (2007) Clockwise exhumation path of granulitized eclogites from the Ama Drime range (Eastern Himalayas). *J Metamorph Geol* 25(1):51–75. doi:[10.1111/j.1525-1314.2006.00678.x](https://doi.org/10.1111/j.1525-1314.2006.00678.x)
- Groppo C, Rolfo F, Lombardo B (2009) P–T evolution across the Main Central Thrust Zone (Eastern Nepal): hidden discontinuities revealed by petrology. *J Petrol* 50(6):1149–1180. doi:[10.1093/petrology/egp036](https://doi.org/10.1093/petrology/egp036)
- Groppo C, Rubatto D, Rolfo F, Lombardo B (2010) Early Oligocene partial melting in the Main Central Thrust Zone (Arun valley, eastern Nepal Himalaya). *Lithos* 118(3–4):287–301. doi:[10.1016/j.lithos.2010.05.003](https://doi.org/10.1016/j.lithos.2010.05.003)
- Groppo C, Rolfo F, Indares A (2012) Partial melting in the higher Himalayan Crystallines of Eastern Nepal: the effect of decompression and implications for the ‘channel flow’ model. *J Petrol* 53(5):1057–1088. doi:[10.1093/petrology/egs009](https://doi.org/10.1093/petrology/egs009)
- Grujic D, Warren CJ, Wooden JL (2011) Rapid synconvergent exhumation of Miocene-aged lower orogenic crust in the eastern Himalaya. *Lithosphere* 3(5):346–366. doi:[10.1130/l154.1](https://doi.org/10.1130/l154.1)
- Harley SL, Nandakumar V (2014) Accessory mineral behaviour in granulite migmatites: a case study from the Kerala Khondalite Belt, India. *J Petrol* 55(10):1965–2002. doi:[10.1093/petrology/egu047](https://doi.org/10.1093/petrology/egu047)
- Harrison TM, McKeegan KD, LeFort P (1995) Detection of inherited monazite in the Manaslu leucogranite by $^{208}\text{Pb}/^{232}\text{Th}$ ion microprobe dating: crystallization age and tectonic implications. *Earth Planet Sci Lett* 133(3–4):271–282. doi:[10.1016/0012-821X\(95\)00091-P](https://doi.org/10.1016/0012-821X(95)00091-P)
- Harrison TM, Grove M, Lovera OM, Catlos EJ (1998) A model for the origin of Himalayan anatexis and inverted metamorphism. *J Geophys Res* 103(B11):27017. doi:[10.1029/98jb02468](https://doi.org/10.1029/98jb02468)
- Hensen BJ (1971) Theoretical phase relations involving cordierite and garnet in the system $\text{MgO}–\text{FeO}–\text{Al}_2\text{O}_3–\text{SiO}_2$. *Contrib Miner Petrol* 33(3):191–214. doi:[10.1007/BF00374063](https://doi.org/10.1007/BF00374063)
- Hokada T, Motoyoshi Y (2006) Electron microprobe technique for U–Th–Pb and REE chemistry of monazite, and its implications for pre-, peak- and post-metamorphic events of the Lutzow-Holm Complex and the Napier Complex, East Antarctica. *Polar Geosci* 19:118–151
- Holdaway M (2000) Application of new experimental and garnet Margules data to the garnet-biotite geothermometer. *Am Mineral* 85(7–8):881–892. doi:[10.2138/am-2000-0701](https://doi.org/10.2138/am-2000-0701)
- Holdaway M (2001) Recalibration of the GASP geobarometer in light of recent garnet and plagioclase activity models and versions of the garnet-biotite geothermometer. *Am Miner* 86(10):1117–1129. doi:[10.2138/am-2001-1001](https://doi.org/10.2138/am-2001-1001)
- Imayama T, Takeshita T, Arita K (2010) Metamorphic P–T profile and P–T path discontinuity across the far-eastern Nepal Himalaya: investigation of channel flow models. *J Metamorph Geol* 28(5):527–549. doi:[10.1111/j.1525-1314.2010.00879.x](https://doi.org/10.1111/j.1525-1314.2010.00879.x)
- Imayama T, Takeshita T, Yi K, Cho D-L, Kitajima K, Tsutsumi Y, Kayama M, Nishido H, Okumura T, Yagi K, Itaya T, Sano Y (2012) Two-stage partial melting and contrasting cooling history within the Higher Himalayan Crystalline Sequence in the far-eastern Nepal Himalaya. *Lithos* 134–135:1–22. doi:[10.1016/j.lithos.2011.12.004](https://doi.org/10.1016/j.lithos.2011.12.004)
- Jamieson RA, Beaumont C, Medvedev S, Nguyen MH (2004) Crustal channel flows: 2. Numerical models with implications for metamorphism in the Himalayan-Tibetan orogen. *J Geophys Res Solid Earth* 109(B6):B06407. doi:[10.1029/2003JB002811](https://doi.org/10.1029/2003JB002811)
- Janasi VdA, Alves A, Vlach SRF, Leite RJ (2003) Granitos Peraluminosos da Porção Central da Faixa Ribeira, Estado de São Paulo: sucessivos eventos de reciclagem da crosta continental no Neoproterozóico. *Geol USP Série Científica São Paulo* 3:13–24. doi:[10.5327/S1519-874X2003000100002](https://doi.org/10.5327/S1519-874X2003000100002)
- Janots E, Brunet F, Goffé B, Poinssot C, Burchard M, Cemič L (2007) Thermochemistry of monazite-(La) and dissakisite-(La): implications for monazite and allanite stability in metapelites. *Contrib Miner Petrol* 154(1):1–14. doi:[10.1007/s00410-006-0176-2](https://doi.org/10.1007/s00410-006-0176-2)
- Jessup MJ, Newell DL, Cottle JM, Berger AL, Spotila JA (2008) Orogen-parallel extension and exhumation enhanced by denudation in the trans-Himalayan Arun River gorge, Ama Drime Massif, Tibet–Nepal. *Geology* 36(7):587–590. doi:[10.1130/g24722a.1](https://doi.org/10.1130/g24722a.1)
- Jiao S, Guo J (2011) Application of the two-feldspar geothermometer to ultrahigh-temperature (UHT) rocks in the Khondalite belt, North China craton and its implications. *Am Miner* 96(2–3):250–260. doi:[10.2138/am.2011.3500](https://doi.org/10.2138/am.2011.3500)
- Kali E, Leloup PH, Arnaud N, Maheo G, Liu DY, Boutonnet E, Van der Woerd J, Liu XH, Jing LZ, Li HB (2010) Exhumation history of the deepest central Himalayan rocks, Ama Drime range: Key pressure-temperature-deformation-time constraints on orogenic models. *Tectonics* 29:TC2014. doi:[10.1029/2009tc002551](https://doi.org/10.1029/2009tc002551)
- Kellett DA, Cottle JM, Smit M (2014) Eocene deep crust at Ama Drime, Tibet: early evolution of the Himalayan orogen. *Lithosphere* 6(4):220–229. doi:[10.1130/l350.1](https://doi.org/10.1130/l350.1)
- Kelly NM, Harley SL, Möller A (2012) Complexity in the behavior and recrystallization of monazite during high-T metamorphism and fluid infiltration. *Chem Geol* 322–323:192–208. doi:[10.1016/j.chemgeo.2012.07.001](https://doi.org/10.1016/j.chemgeo.2012.07.001)
- Kelsey DE, Hand M (2015) On ultrahigh temperature crustal metamorphism: phase equilibria, trace element thermometry, bulk composition, heat sources, timescales and tectonic settings. *Geosci Front* 6(3):311–356. doi:[10.1016/j.gsf.2014.09.006](https://doi.org/10.1016/j.gsf.2014.09.006)
- Kelsey DE, Clark C, Hand M (2008) Thermobarometric modelling of zircon and monazite growth in melt-bearing systems: examples using model metapelitic and metapsammite granulites. *J Metamorph Geol* 26(2):199–212. doi:[10.1111/j.1525-1314.2007.00757.x](https://doi.org/10.1111/j.1525-1314.2007.00757.x)
- Kingsbury JA, Miller CF, Wooden JL, Harrison TM (1993) Monazite paragenesis and U–Pb systematics in rocks of the eastern Mojave Desert, California, USA: implications for thermochronometry. *Chem Geol* 110(1):147–167. doi:[10.1016/0009-2541\(93\)90251-D](https://doi.org/10.1016/0009-2541(93)90251-D)
- Kohn MJ (2008) P–T–t data from central Nepal support critical taper and repudiate large-scale channel flow of the Greater Himalayan sequence. *Geol Soc Am Bull* 120(3–4):259–273. doi:[10.1130/b26252.1](https://doi.org/10.1130/b26252.1)
- Kohn MJ (2014) Himalayan metamorphism and its tectonic implications. *Annu Rev Earth Planet Sci* 42:381–419. doi:[10.1146/annurev-earth-060313-055005](https://doi.org/10.1146/annurev-earth-060313-055005)
- Kohn MJ (2016) Metamorphic chronology—a tool for all ages: past achievements and future prospects. *Am Mineral* 101(1):25–42. doi:[10.2138/am-2016-5146](https://doi.org/10.2138/am-2016-5146)
- Kohn MJ, Malloy MA (2004) Formation of monazite via prograde metamorphic reactions among common silicates: implications for age determinations. *Geochim Cosmochim Acta* 68(1):101–113. doi:[10.1016/s0016-7037\(03\)00258-8](https://doi.org/10.1016/s0016-7037(03)00258-8)
- Kohn MJ, Wieland MS, Parkinson CD, Upreti BN (2004) Miocene faulting at plate tectonic velocity in the Himalaya of central Nepal. *Earth Planet Sci Lett* 228(3–4):299–310. doi:[10.1016/j.epsl.2004.10.007](https://doi.org/10.1016/j.epsl.2004.10.007)
- Kohn MJ, Wieland MS, Parkinson CD, Upreti BN (2005) Five generations of monazite in Langtang gneisses: implications for

- chronology of the Himalayan metamorphic core. *J Metamorph Geol* 23(5):399–406. doi:[10.1111/j.1525-1314.2005.00584.x](https://doi.org/10.1111/j.1525-1314.2005.00584.x)
- Kooijman E, Smit MA, Mezger K, Berndt J (2012) Trace element systematics in granulite facies rutile: implications for Zr geothermometry and provenance studies. *J Metamorph Geol* 30(4):397–412. doi:[10.1111/j.1525-1314.2012.00972.x](https://doi.org/10.1111/j.1525-1314.2012.00972.x)
- Larson KP, Gervais F, Kellett DA (2013) A P-T-t-D discontinuity in east-central Nepal: implications for the evolution of the Himalayan mid-crust. *Lithos* 179:275–292. doi:[10.1016/j.lithos.2013.08.012](https://doi.org/10.1016/j.lithos.2013.08.012)
- Larson KP, Ambrose TK, Webb AG, Cottle JM, Shrestha S (2015) Reconciling Himalayan midcrustal discontinuities: the Main Central thrust system. *Earth Planet Sci Lett* 429:139–146. doi:[10.1016/j.jsg.2015.06.008](https://doi.org/10.1016/j.jsg.2015.06.008)
- Le Breton N, Thompson AB (1988) Fluid-absent (dehydration) melting of biotite in metapelites in the early stages of crustal anatexis. *Contrib Miner Petrol* 99(2):226–237. doi:[10.1007/bf00371463](https://doi.org/10.1007/bf00371463)
- Leech M, Singh S, Jain A, Klemperer S, Manickavasagam R (2005) The onset of India-Asia continental collision: early, steep subduction required by the timing of UHP metamorphism in the western Himalaya. *Earth Planet Sci Lett* 234(1–2):83–97. doi:[10.1016/j.epsl.2005.02.038](https://doi.org/10.1016/j.epsl.2005.02.038)
- Leloup PH, Mahéo G, Arnaud N, Kali E, Boutonnet E, Liu D, Xiaohan L, Haibing L (2010) The South Tibet detachment shear zone in the Dinggye area Time constraints on extrusion models of the Himalayas. *Earth Planet Sci Lett* 292(1–2):1–16. doi:[10.1016/j.epsl.2009.12.035](https://doi.org/10.1016/j.epsl.2009.12.035)
- Leloup PH, Liu X, Mahéo G, Paquette J-L, Arnaud N, Aubray A, Liu X (2015) New constraints on the timing of partial melting and deformation along the Nyalam section (central Himalaya): implications for extrusion models. *Geol Soc Lond Spec Public* 412(1):131–175. doi:[10.1144/sp412.11](https://doi.org/10.1144/sp412.11)
- Li D, Liao Q, Yuan Y, Wan Y, Liu D, Zhang X, Yi S, Cao S, Xie D (2003) SHRIMP U–Pb zircon geochronology of granulites at Rimana (Southern Tibet) in the central segment of Himalayan orogen. *Chin Sci Bull* 48(23):2647–2650. doi:[10.1360/03wd0080](https://doi.org/10.1360/03wd0080)
- Li XH, Liu Y, Li QL, Guo CH, Chamberlain KR (2009) Precise determination of Phanerozoic zircon Pb/Pb age by multicollector SIMS without external standardization. *Geochem Geophys Geosyst* 10(4). doi:[10.1029/2009GC002400](https://doi.org/10.1029/2009GC002400)
- Li Q-L, Li X-H, Liu Y, Tang G-Q, Yang J-H, Zhu W-G (2010) Precise U–Pb and Pb–Pb dating of Phanerozoic baddeleyite by SIMS with oxygen flooding technique. *J Anal At Spectrom* 25(7):1107–1113. doi:[10.1039/B923444F](https://doi.org/10.1039/B923444F)
- Li X, Tang G, Gong B, Yang Y, Hou K, Hu Z, Li Q, Liu Y, Li W (2013) Qinghu zircon: a working reference for microbeam analysis of U–Pb age and Hf and O isotopes. *Chin Sci Bull* 58(36):4647–4654. doi:[10.1007/s11434-013-5932-x](https://doi.org/10.1007/s11434-013-5932-x)
- Liu Y, Siebel W, Massonne HJ, Xiao XC (2007) Geochronological and petrological constraints for tectonic evolution of the central Greater Himalayan Sequence in the Kharta area, southern Tibet. *J Geol* 115(2):215–230. doi:[10.1086/510806](https://doi.org/10.1086/510806)
- Lombardo B, Rolfo F (2000) Two contrasting eclogite types in the Himalayas: implications for the Himalayan orogeny. *J Geodyn* 30(1–2):37–60. doi:[10.1016/S0264-3707\(99\)00026-5](https://doi.org/10.1016/S0264-3707(99)00026-5)
- Lombardo B, Rolfo F, McClelland WC (2016) A review of the first eclogites discovered in the Eastern Himalaya. *Eur J Miner* 28:1099–1109. doi:[10.1127/ejm/2016/0028-2553](https://doi.org/10.1127/ejm/2016/0028-2553)
- Ludwig KR (2008) Isoplot/Ex version 3.7. A geochronological toolkit for Microsoft Excel. Berkeley Geochronological Centre, Special Publication. http://www.bgc.org/isoplot_etc/isoplot.html
- Martin AJ, Gehrels GE, DeCelles PG (2007) The tectonic significance of (U, Th)/Pb ages of monazite inclusions in garnet from the Himalaya of central Nepal. *Chem Geol* 244(1–2):1–24. doi:[10.1016/j.chemgeo.2007.05.003](https://doi.org/10.1016/j.chemgeo.2007.05.003)
- McDonough WF, Ss Sun (1995) The composition of the Earth. *Chem Geol* 120(3–4):223–253. doi:[10.1016/0009-2541\(94\)00140-4](https://doi.org/10.1016/0009-2541(94)00140-4)
- Montel J-M (1993) A model for monazite/melt equilibrium and application to the generation of granitic magmas. *Chem Geol* 110(1):127–146. doi:[10.1016/0009-2541\(93\)90250-M](https://doi.org/10.1016/0009-2541(93)90250-M)
- Montomoli C, Iaccarino S, Carosi R, Langone A, Visonà D (2013) Tectonometamorphic discontinuities within the Greater Himalayan Sequence in Western Nepal (Central Himalaya): insights on the exhumation of crystalline rocks. *Tectonophysics* 608:1349–1370. doi:[10.1016/j.tecto.2013.06.006](https://doi.org/10.1016/j.tecto.2013.06.006)
- Montomoli C, Carosi R, Iaccarino S (2015) Tectonometamorphic discontinuities in the Greater Himalayan Sequence: a local or a regional feature? *Geol Soc Lond Spec Public* 412(1):25–41. doi:[10.1144/sp412.3](https://doi.org/10.1144/sp412.3)
- Mottram CM, Warren CJ, Regis D, Roberts NMW, Harris NBW, Argles TW, Parrish RR (2014) Developing an inverted Barrovian sequence; insights from monazite petrochronology. *Earth Planet Sci Lett* 403:418–431. doi:[10.1016/j.epsl.2014.07.006](https://doi.org/10.1016/j.epsl.2014.07.006)
- Ouzegane K, Boumaza S (1996) An example of ultrahigh-temperature metamorphism: orthopyroxene–sillimanite–garnet, sapphirine–quartz and spinel–quartz parageneses in Al–Mg granulites from In Hihaou, In Ouzzal, Hoggar. *J Metamorph Geol* 14(6):693–708. doi:[10.1111/j.1525-1314.1996.00049.x](https://doi.org/10.1111/j.1525-1314.1996.00049.x)
- Parrish RR (1990) U–Pb dating of monazite and its application to geological problems. *Can J Earth Sci* 27(11):1431–1450. doi:[10.1139/e90-152](https://doi.org/10.1139/e90-152)
- Pearce NJG, Perkins WT, Westgate JA, Gorton MP, Jackson SE, Neal CR, Chenery SP (1997) A compilation of new and published major and trace element data for NIST SRM 610 and NIST SRM 612 glass reference materials. *Geostand News* 21(1):115–144. doi:[10.1111/j.1751-908X.1997.tb00538.x](https://doi.org/10.1111/j.1751-908X.1997.tb00538.x)
- Peterman EM, Mattinson JM, Hacker BR (2012) Multi-step TIMS and CA-TIMS monazite U–Pb geochronology. *Chem Geol* 312–313:58–73. doi:[10.1016/j.chemgeo.2012.04.006](https://doi.org/10.1016/j.chemgeo.2012.04.006)
- Pyle JM, Spear FS, Rudnick RL, McDonough WF (2001) Monazite–xenotime–garnet equilibrium in metapelites and a new monazite–garnet thermometer. *J Petrol* 42(11):2083–2107. doi:[10.1093/ptrology/42.11.2083](https://doi.org/10.1093/ptrology/42.11.2083)
- Rapp RP, Watson EB (1986) Monazite solubility and dissolution kinetics: implications for the thorium and light rare earth chemistry of felsic magmas. *Contrib Miner Petrol* 94(3):304–316. doi:[10.1007/bf00371439](https://doi.org/10.1007/bf00371439)
- Rowley DB (1996) Age of initiation of collision between India and Asia: a review of stratigraphic data. *Earth Planet Sci Lett* 145(1–4):1–13. doi:[10.1016/S0012-821X\(96\)00201-4](https://doi.org/10.1016/S0012-821X(96)00201-4)
- Rubatto D, Williams IS, Buick IS (2001) Zircon and monazite response to prograde metamorphism in the Reynolds Range, central Australia. *Contrib Miner Petrol* 140(4):458–468. doi:[10.1007/PL00007673](https://doi.org/10.1007/PL00007673)
- Rubatto D, Hermann J, Buick IS (2006) Temperature and bulk composition control on the growth of monazite and zircon during low-pressure anatexis (Mount Stafford, central Australia). *J Petrol* 47(10):1973–1996. doi:[10.1093/ptrology/egl033](https://doi.org/10.1093/ptrology/egl033)
- Rubatto D, Chakraborty S, Dasgupta S (2013) Timescales of crustal melting in the Higher Himalayan Crystallines (Sikkim, Eastern Himalaya) inferred from trace element-constrained monazite and zircon chronology. *Contrib Miner Petrol* 165(2):349–372. doi:[10.1007/s00410-012-0812-y](https://doi.org/10.1007/s00410-012-0812-y)
- Schaltegger U, Fanning CM, Günther D, Maurin JC, Schulmann K, Gebauer D (1999) Growth, annealing and recrystallization of zircon and preservation of monazite in high-grade metamorphism: conventional and in situ U–Pb isotope, cathodoluminescence and microchemical evidence. *Contrib Miner Petrol* 134(2–3):186–201. doi:[10.1007/s004100050478](https://doi.org/10.1007/s004100050478)
- Schandl ES, Gorton MP (2004) A textural and geochemical guide to the identification of hydrothermal monazite: criteria for selection

- of samples for dating epigenetic hydrothermal ore deposits. *Econ Geol* 99(5):1027–1035. doi:[10.2113/gsecongeo.99.5.1027](https://doi.org/10.2113/gsecongeo.99.5.1027)
- Schärer U (1984) The effect of initial ^{230}Th disequilibrium on young U–Pb ages: the Makalu case, Himalaya. *Earth Planet Sci Lett* 67(2):191–204. doi:[10.1016/0012-821X\(84\)90114-6](https://doi.org/10.1016/0012-821X(84)90114-6)
- Schelling D (1992) The tectonostratigraphy and structure of the eastern Nepal Himalaya. *Tectonics* 11(5):925–943. doi:[10.1029/92TC00213](https://doi.org/10.1029/92TC00213)
- Searle MP, Szulc AG (2005) Channel flow and ductile extrusion of the high Himalayan slab—the Kangchenjunga–Darjeeling profile, Sikkim Himalaya. *J Asian Earth Sci* 25(1):173–185. doi:[10.1016/j.jseaes.2004.03.004](https://doi.org/10.1016/j.jseaes.2004.03.004)
- Searle MP, Parrish RR, Hodges KV, Hurford A, Ayres MW, Whitehouse MJ (1997) Shisha Pangma leucogranite, south Tibetan Himalaya: field relations, geochemistry, age, origin, and emplacement. *J Geol* 105(3):295–317. doi:[10.1086/515924](https://doi.org/10.1086/515924)
- Searle MP, Simpson RL, Law RD, Parrish RR, Waters DJ (2003) The structural geometry, metamorphic and magmatic evolution of the Everest massif, High Himalaya of Nepal–South Tibet. *J Geol Soc* 160(3):345–366. doi:[10.1144/0016-764902-126](https://doi.org/10.1144/0016-764902-126)
- Searle MP, Law RD, Godin L, Larson KP, Streule MJ, Cottle JM, Jessup MJ (2008) Defining the Himalayan Main Central Thrust in Nepal. *J Geol Soc* 165(2):523–534. doi:[10.1144/0016-76492007-081](https://doi.org/10.1144/0016-76492007-081)
- Seydoux-Guillaume AM, Paquette J-L, Wiedenbeck M, Montel J-M, Heinrich W (2002) Experimental resetting of the U–Th–Pb systems in monazite. *Chem Geol* 191(1–3):165–181. doi:[10.1016/S0009-2541\(02\)00155-9](https://doi.org/10.1016/S0009-2541(02)00155-9)
- Simpson RL, Parrish RR, Searle MP, Waters DJ (2000) Two episodes of monazite crystallization during metamorphism and crustal melting in the Everest region of the Nepalese Himalaya. *Geology* 28(5):403. doi:[10.1130/0091-7613\(2000\)28<403:teomcd>2.0.co;2](https://doi.org/10.1130/0091-7613(2000)28<403:teomcd>2.0.co;2)
- Sláma J, Košler J, Condon DJ, Crowley JL, Gerdes A, Hanchar JM, Horstwood MSA, Morris GA, Nasdala L, Norberg N, Schaltegger U, Schoene B, Tubrett MN, Whitehouse MJ (2008) Plešovice zircon—a new natural reference material for U–Pb and Hf isotopic microanalysis. *Chem Geol* 249(1–2):1–35. doi:[10.1016/j.chemgeo.2007.11.005](https://doi.org/10.1016/j.chemgeo.2007.11.005)
- Smith HA, Barreiro B (1990) Monazite U–Pb dating of staurolite grade metamorphism in pelitic schists. *Contrib Miner Petrol* 105(5):602–615. doi:[10.1007/BF00302498](https://doi.org/10.1007/BF00302498)
- Smith M, Henderson P, Campbell L (2000) Fractionation of the REE during hydrothermal processes: constraints from the Bayan Obo Fe–REE–Nb deposit, Inner Mongolia, China. *Geochim Cosmochim Acta* 64(18):3141–3160. doi:[10.1016/S0016-7037\(00\)00416-6](https://doi.org/10.1016/S0016-7037(00)00416-6)
- Sorcar N, Hoppe U, Dasgupta S, Chakraborty S (2014) High-temperature cooling histories of migmatites from the High Himalayan Crystallines in Sikkim, India: rapid cooling unrelated to exhumation? *Contrib Miner Petrol* 167(2):1–34. doi:[10.1007/s00410-013-0957-3](https://doi.org/10.1007/s00410-013-0957-3)
- Spear FS, Kohn MJ, Cheney JT (1999) P–T paths from anatectic pelites. *Contrib Miner Petrol* 134(1):17–32. doi:[10.1007/s004100050466](https://doi.org/10.1007/s004100050466)
- Stacey JS, Kramers JD (1975) Approximation of terrestrial lead isotope evolution by a two-stage model. *Earth Planet Sci Lett* 26(2):207–221. doi:[10.1016/0012-821X\(75\)90088-6](https://doi.org/10.1016/0012-821X(75)90088-6)
- Steiger RH, Jäger E (1977) Subcommittee on geochronology: convention on the use of decay constants in geo- and cosmochronology. *Earth Planet Sci Lett* 36(3):359–362. doi:[10.1016/0012-821X\(77\)90060-7](https://doi.org/10.1016/0012-821X(77)90060-7)
- Stepanov AS, Hermann J, Rubatto D, Rapp RP (2012) Experimental study of monazite/melt partitioning with implications for the REE, Th and U geochemistry of crustal rocks. *Chem Geol* 300–301:200–220. doi:[10.1016/j.chemgeo.2012.01.007](https://doi.org/10.1016/j.chemgeo.2012.01.007)
- Taylor RJM, Clark C, Fitzsimons ICW, Santosh M, Hand M, Evans N, McDonald B (2014) Post-peak, fluid-mediated modification of granulite facies zircon and monazite in the Trivandrum Block, southern India. *Contrib Miner Petrol* 168(2):1044. doi:[10.1007/s00410-014-1044-0](https://doi.org/10.1007/s00410-014-1044-0)
- Taylor RJM, Kirkland CL, Clark C (2016) Accessories after the facts: constraining the timing, duration and conditions of high-temperature metamorphic processes. *Lithos* 264:239–257. doi:[10.1016/j.lithos.2016.09.004](https://doi.org/10.1016/j.lithos.2016.09.004)
- Tomkins HS, Powell R, Ellis DJ (2007) The pressure dependence of the zirconium-in-rutile thermometer. *J Metamorph Geol* 25(6):703–713. doi:[10.1111/j.1525-1314.2007.00724.x](https://doi.org/10.1111/j.1525-1314.2007.00724.x)
- Visonà D, Lombardo B (2002) Two-mica and tourmaline leucogranites from the Everest–Makalu region (Nepal–Tibet). Himalayan leucogranite genesis by isobaric heating? *Lithos* 62(3–4):125–150. doi:[10.1016/s0024-4937\(02\)00112-3](https://doi.org/10.1016/s0024-4937(02)00112-3)
- Wang X, Zhang J, Santosh M, Liu J, Yan S, Guo L (2012) Andean-type orogeny in the Himalayas of south Tibet: Implications for early Paleozoic tectonics along the Indian margin of Gondwana. *Lithos* 154:248–262. doi:[10.1016/j.lithos.2012.07.011](https://doi.org/10.1016/j.lithos.2012.07.011)
- Wang JM, Zhang JJ, Wang XX (2013) Structural kinematics, metamorphic P–T profiles and zircon geochronology across the Greater Himalayan Crystalline Complex in south-central Tibet: implication for a revised channel flow. *J Metamorph Geol* 31(6):607–628. doi:[10.1111/jmg.12036](https://doi.org/10.1111/jmg.12036)
- Wang J-M, Rubatto D, Zhang J-J (2015a) Timing of Partial Melting and Cooling across the Greater Himalayan Crystalline Complex (Nyalam, Central Himalaya): in-sequence Thrusting and its Implications. *J Petrol* 56(9):1677–1702. doi:[10.1093/petrology/egv050](https://doi.org/10.1093/petrology/egv050)
- Wang JM, Zhang JJ, Wei CJ, Rai SM, Wang M, Qian JH (2015b) Characterising the metamorphic discontinuity across the Main Central Thrust Zone of eastern-central Nepal. *J Asian Earth Sci* 101:83–100. doi:[10.1016/j.jseaes.2015.01.027](https://doi.org/10.1016/j.jseaes.2015.01.027)
- Wang J-M, Zhang J-J, Liu K, Zhang B, Wang X-X, Rai S, Scheltens M (2016) Spatial and temporal evolution of tectonometamorphic discontinuities in the central Himalaya: constraints from P–T paths and geochronology. *Tectonophysics* 679:41–60. doi:[10.1016/j.tecto.2016.04.035](https://doi.org/10.1016/j.tecto.2016.04.035)
- Wang Y, Zhang L, Zhang J, Wei C (2017) The youngest eclogite in central Himalaya: P–T path, U–Pb zircon age and its tectonic implication. *Gondwana Res* 41:188–206. doi:[10.1016/j.gr.2015.10.013](https://doi.org/10.1016/j.gr.2015.10.013)
- Warren CJ, Grujic D, Kellett DA, Cottle J, Jamieson RA, Ghalley KS (2011) Probing the depths of the India–Asia collision: U–Th–Pb monazite chronology of granulites from NW Bhutan. *Tectonics* 30(2):TC2004. doi:[10.1029/2010TC002738](https://doi.org/10.1029/2010TC002738)
- Warren CJ, Singh AK, Roberts NMW, Regis D, Halton AM, Singh RB (2014) Timing and conditions of peak metamorphism and cooling across the Zimithang Thrust, Arunachal Pradesh, India. *Lithos* 200–201:94–110. doi:[10.1016/j.lithos.2014.04.005](https://doi.org/10.1016/j.lithos.2014.04.005)
- Watson EB, Wark DA, Thomas JB (2006) Crystallization thermometers for zircon and rutile. *Contrib Miner Petrol* 151(4):413–433. doi:[10.1007/s00410-006-0068-5](https://doi.org/10.1007/s00410-006-0068-5)
- Whitney DL, Evans BW (2010) Abbreviations for names of rock-forming minerals. *Am Miner* 95(1):185–187. doi:[10.2138/am.2010.3371](https://doi.org/10.2138/am.2010.3371)
- Wiedenbeck M, Allé P, Corfu F, Griffin WL, Meier M, Oberli F, Quadt AV, Roddick JC, Spiegel W (1995) Three natural zircon standards for U–Th–Pb, Lu–Hf, trace element and REE analyses. *Geostand News* 19(1):1–23. doi:[10.1111/j.1751-908X.1995.tb00147.x](https://doi.org/10.1111/j.1751-908X.1995.tb00147.x)
- Williams IS (1998) U–Th–Pb geochronology by ion microprobe. In: McKibben MA, Shanks III WC, and Ridley WI (eds.), Applications of microanalytical techniques to understanding mineralizing processes. *Rev Econ Geol* 7:1–35

- Williams ML, Jercinovic MJ, Hetherington CJ (2007) Microprobe monazite geochronology: understanding geologic processes by integrating composition and chronology. *Annu Rev Earth Planet Sci* 35:137–175. doi:[10.1146/annurev.earth.35.031306.140228](https://doi.org/10.1146/annurev.earth.35.031306.140228)
- Williams ML, Jercinovic MJ, Harlov DE, Budzyń B, Hetherington CJ (2011) Resetting monazite ages during fluid-related alteration. *Chem Geol* 283(3–4):218–225. doi:[10.1016/j.chemgeo.2011.01.019](https://doi.org/10.1016/j.chemgeo.2011.01.019)
- Wing BA, Ferry JM, Harrison TM (2003) Prograde destruction and formation of monazite and allanite during contact and regional metamorphism of pelites: petrology and geochronology. *Contrib Miner Petrol* 145(2):228–250. doi:[10.1007/s00410-003-0446-1](https://doi.org/10.1007/s00410-003-0446-1)
- Wu C-M, Zhang J, Ren L-D (2004) Empirical garnet–biotite–plagioclase–quartz (GBPQ) geobarometry in medium-to high-grade metapelites. *J Petrol* 45(9):1907–1921. doi:[10.1093/petrology/egh038](https://doi.org/10.1093/petrology/egh038)
- Wu FY, Liu ZC, Liu XC, Ji WQ (2015) Himalayan leucogranite: petrogenesis and implications to orogenesis and plateau uplift. *Acta Petrol Sin* 31(1):1–36 (**In Chinese with English abstract**)
- Yakymchuk C, Brown M (2014) Behaviour of zircon and monazite during crustal melting. *J Geol Soc* 171(4):465–479. doi:[10.1144/jgs2013-115](https://doi.org/10.1144/jgs2013-115)
- Yin A (2006) Cenozoic tectonic evolution of the Himalayan orogen as constrained by along-strike variation of structural geometry, exhumation history, and foreland sedimentation. *Earth Sci Rev* 76:1–131. doi:[10.1016/j.earscirev.2005.05.004](https://doi.org/10.1016/j.earscirev.2005.05.004)
- Zhang JJ, Guo L (2007) Structure and geochronology of the southern Xainza-Dinggye rift and its relationship to the south Tibetan detachment system. *J Asian Earth Sci* 29(5–6):722–736. doi:[10.1016/j.jseae.2006.05.003](https://doi.org/10.1016/j.jseae.2006.05.003)
- Zhang ZM, Dong X, Xiang H, Liou JG, Santosh M (2013) Building of the Deep Gangdese Arc, South Tibet: Paleocene Plutonism and Granulite-Facies Metamorphism. *J Petrol* 54(12):2547–2580. doi:[10.1093/petrology/egt056](https://doi.org/10.1093/petrology/egt056)
- Zhang ZM, Xiang H, Dong X, Li W, Ding HX, Gou Z, Tian ZL (2017) Oligocene HP metamorphism and anatexis of the Higher Himalayan Crystalline Sequence in Yadong region, east-central Himalaya. *Gondwana Res* 41:173–187. doi:[10.1016/j.gr.2015.03.002](https://doi.org/10.1016/j.gr.2015.03.002)
- Zhu XK, O’Nions RK (1999) Monazite chemical composition: some implications for monazite geochronology. *Contrib Miner Petrol* 137(4):351–363. doi:[10.1007/s004100050555](https://doi.org/10.1007/s004100050555)